

# The importance of transient resonances in extreme-mass-ratio inspirals (new title?)

Robert H. Cole,<sup>1</sup> Christopher P.L. Berry,<sup>2,1,\*</sup> Priscilla Cañizares,<sup>1</sup> and Jonathan R. Gair<sup>1</sup>

<sup>1</sup>*Institute of Astronomy, Madingley Road, Cambridge, CB3 0HA, United Kingdom*

<sup>2</sup>*School of Physics and Astronomy, University of Birmingham, Edgbaston, Birmingham B15 2TT, United Kingdom*

(Dated: June 29, 2015)

*Update abstract* The inspiral of stellar-mass compact objects into supermassive black holes provides a wealth of information about the strong gravitational-field regime via the emission of gravitational waves. In order to detect such signals and extract the desired information, it is necessary to possess a bank of accurate waveform templates. For computational efficiency, adiabatic templates are often used, which accurately reproduce orbit-averaged trajectories arising from the first order dissipative gravitational self-force. Other effects are however neglected, in particular that of transient resonances, where the radial and poloidal fundamental frequencies become commensurate. During such resonances, the flux of gravitational waves can be diminished or enhanced, leading to a shift in the compact-object trajectory and, ultimately, the phase of the emitted radiation. In this work, an astrophysical population of detectable extreme-mass-ratio inspirals is studied and it is found that a large proportion shall encounter a low-order resonance in the later stages of inspiral. The resulting effect on signal-to-noise recovery is small due to the low eccentricity of the studied population, but nevertheless at least one fifth of the systems may become undetectable if transient resonances are not accounted for.

PACS numbers: 04.25.Nx, 04.30.-w, 04.70.-s, 98.62.Js

## I. INTRODUCTION

In the prologue to his classic monograph, Chandrasekhar [1] celebrates the simplicity of black holes (BHs). The Kerr solution is defined by just two parameters: mass and spin. Despite the baldness of the BH metrics, great intricacies manifest in their properties. This is made evident when a second body is introduced. The two-body problem in general relativity (GR) is well studied. It is of paramount importance for gravitational-wave (GW) astronomy, where binary systems are the dominant source of radiation. Correctly modelling the dynamics of these systems is necessary to interpret and extract information from gravitational waveforms.

We have made progress in understanding the general relativistic two-body problem in recent years. Bodies of comparable mass can be studied using numerical relativity. Rapid advances in this field have been made following breakthroughs in 2005 [2–4]; it is now possible to simulate hundreds of orbits [5]. These simulations allow us to understand BH–BH mergers. Stellar-mass BH mergers are targets for ground-based GW detectors, such as the upcoming Advanced LIGO [6] and Virgo [7], and the in-construction KAGRA [8]. Massive BH mergers, expected to be the result of galaxy mergers, are potential sources for a space-borne detector such as eLISA [9]. Systems of unequal masses are more challenging to evolve numerically as they complete a larger number of orbits and it is necessary to resolve two different scales. Calculations can instead be performed perturbatively. The paradigm

unequal-mass system has a stellar-mass BH orbiting a massive black hole, such as those expected to be found at the centre of most galaxies. These extreme-mass-ratio inspirals (EMRIs) produce GWs that are a promising signal for space-borne detectors [10]. Despite being well-studied there still remain open questions.

In the case of extreme-mass-ratio systems, efforts are concentrated on understanding the gravitational self-force [11, 12]. In the test particle limit, the smaller body follows an exact geodesic of the BH’s spacetime. Including the effects of the smaller body’s finite mass, the background spacetime is perturbed. The back-reaction from this deformation alters the small body’s orbital trajectory, and can be modelled as a self-force that moves the body from its geodesic. The self-force is commonly divided into two pieces, dissipative and conservative. The former encapsulates the slow decay of the orbital energy and angular momentum, constants of the motion in the test particle limit, through radiation. The latter shifts the orbital phases inducing precession. The dissipative piece is time-asymmetric and has the larger effect on the evolution of the orbital phase; the conservative piece is time-symmetric and has a smaller influence on the phase although this can accumulate over many orbits. Being able to accurately model the influence of the self-force allows us to create reliable waveform models.

Flanagan and Hinderer [13] highlighted a previously overlooked phenomenon that occurs in the general relativistic two-body problem, that of transient resonances. Geodesic orbits in GR have three associated frequencies: the radial frequency  $\Omega_r$ , the polar frequency  $\Omega_\theta$  and the azimuthal frequency  $\Omega_\phi$ . The first two describe libration and the third rotation (except in the case of polar orbits where  $\Omega_\theta$  also describes rotation) [14]. In the weak-field limit, these all tend towards the Keplerian frequency; in

---

\*cplb@star.sr.bham.ac.uk

the strong-field,  $\Omega_r < \Omega_\theta < \Omega_\phi$ , and they may differ significantly. For extreme-mass-ratio systems, the evolution time-scale is much longer than the orbital period such that the motion of the smaller body is approximately geodesic over orbital time-scales. The evolution of the orbit can be approximated as a series of geodesics using the osculating element formalism [15, 16]. During this evolution, the frequencies may become commensurate. Resonances occur when the radial and polar frequencies are rational multiples of each other:

$$\nu \equiv \frac{\Omega_r}{\Omega_\theta} = \frac{n_\theta}{n_r}, \quad (1)$$

where  $n_r$  and  $n_\theta$  are integers (with no common factors). During resonance, terms in the self-force that usually average to zero can combine coherently, significantly impacting the orbital motion [17].

Resonances involving the azimuthal motion do not produce a comparable effect because of the axisymmetry of the background spacetime. However, both  $\theta$ - $\phi$  resonances [18] and  $r$ - $\phi$  resonances [19] can lead to extrinsic effects; the GWs from such systems are not emitted isotropically and the imbalance produces a kick velocity that is, in some cases, sufficient to eject the central black hole from its host.

Geodesic motion in Kerr spacetime can be described by use of the action-angle formalism [14]. We consider a body of mass  $\mu$  orbiting a BH of mass  $M$ , with  $\eta = \mu/M \ll 1$ ,<sup>1</sup> and describe the motion in the directions of the standard Boyer-Lindquist coordinates  $\{t, r, \theta, \phi\}$  using generalised angle variables  $q_\alpha = \{q_t, q_r, q_\theta, q_\phi\}$  [20]. We denote the first integrals of the geodesic motion, the generalised action variables, by  $J_\alpha$ . These are some combination of the energy per unit mass  $E$  and the axial angular momentum per unit mass  $L_z$ , which arise from isometries of the metric in  $t$  and  $\phi$ , and the Carter constant per unit mass squared  $Q$  [21], which is related to the separability of the equations of motion in  $r$  and  $\theta$ . The system evolves following [13]

$$\frac{dq_\alpha}{d\lambda} = \omega_\alpha(\mathbf{J}) + \eta g_\alpha^{(1)}(q_r, q_\theta, \mathbf{J}) + \mathcal{O}(\eta^2), \quad (2a)$$

$$\frac{dJ_\alpha}{d\lambda} = \eta G_\alpha^{(1)}(q_r, q_\theta, \mathbf{J}) + \mathcal{O}(\eta^2), \quad (2b)$$

where  $\lambda$  is Mino time [22], and the forcing functions  $g_\alpha^{(1)}$  and  $G_\alpha^{(1)}$  originate from the first-order self-force. By working with  $\lambda$  instead of proper time  $\tau$ , the radial and polar motions decouple. At zeroth order in the mass ratio we recover the limit of purely geodesic motion: the integrals of the motion are actually constants and the angle variables evolve according to their associated frequencies  $\omega_\alpha$ .

The leading-order dissipative correction to geodesic motion is calculated following the adiabatic prescription [20]: by dropping the forcing term  $g_\alpha^{(1)}$  (and all higher-order terms) and replacing the forcing term  $G_\alpha^{(1)}$  with its average over the 2-torus parametrized by  $q_r$  and  $q_\theta$   $\langle G_\alpha^{(1)} \rangle_{q_r, q_\theta}$  [23]. For most orbits this is sufficient,  $G_\alpha^{(1)}$  is given by its average value plus a rapidly oscillating component [24]. However, this averaging fails when the ratio of frequencies is the ratio of integers. In this case the trajectory does not ergodically fill the 2-torus, but instead traces out a 1-dimensional subspace.<sup>2</sup> There are then contributions to the self-force that no longer average out beyond  $\langle G_A^{(1)} \rangle_{q_r, q_\theta}$ . Intuitively, we expect that this effect is more important for ratios of small integers as when the integers are large, the orbit comes close to all points on the 2-torus.

In this work we seek to characterise the importance of these resonances for the purposes of modelling EMRIs. The amplitude of expected signals is below the level of noise in a space-based GW detector. However, systems remain in band for many hundreds of thousands of cycles and so may be detected using a matched filter, provided we have sufficiently accurate waveform templates. Ensuring the accuracy of EMRI templates requires calculating the impact that passing through a resonance has on the orbital evolution and discovering for which resonances this is significant.

In Sec. II, we formulate the specific problem: that of geodesic motion in Kerr spacetime, perturbed by the gravitational self-force. We then study generic properties of transient resonances in Sec. III, detailing their location in parameter space, the time-scales over which they affect the motion and the resulting GW flux enhancements. Specific examples are considered to illustrate the effects of resonances at the start of Sec. IV, before finally turning to an astrophysical population in Sec. IV F. Our conclusions can be found in Sec. V.

We use geometric units with  $G = c = 1$  throughout. We always use  $M$  for the mass of the central massive BH and  $a$  as the spin parameter. We also use the dimensionless spin  $a_* \equiv a/M$ ; we take the convention that  $0 \leq a_* < 1$ .

## II. PROBLEM FORMULATION

### A. Kerr geodesics

The evolution of an extreme-mass-ratio ( $\eta \ll 1$ ) system is slow. Instantaneously, the motion of the orbiting mass can be described as geodesic, with the integrals of the motion changing on time-scales of many orbital periods. We analyse the behaviour of resonances within

<sup>1</sup> To first order, the mass ratio  $\eta$  is the same as the symmetric mass ratio  $\mu M/(\mu + M)^2$ .

<sup>2</sup> For illustrations, see Grossman, Levin and Perez-Giz [25].

the osculating element framework, where the trajectory is described by a sequence of geodesics that each match onto the motion at a particular instance. It is therefore necessary to develop an understanding of the Kerr geodesics.

The geodesic equations may be written as [1, 21]

$$\frac{dt}{d\lambda} = a(L_z - aE \sin^2 \theta) + \frac{r^2 + a^2}{\Delta} \mathcal{T}, \quad (3a)$$

$$\frac{dr}{d\lambda} = \pm \sqrt{V_r}, \quad (3b)$$

$$\frac{d\theta}{d\lambda} = \pm \sqrt{V_\theta}, \quad (3c)$$

$$\frac{d\phi}{d\lambda} = \frac{L_z}{\sin^2 \theta} - aE + \frac{a}{\Delta} \mathcal{T}, \quad (3d)$$

where  $\Delta = r^2 - 2Mr + a^2$ ; the signs of the  $r$  and  $\theta$  equations can be chosen independently, and we have introduced potentials

$$\mathcal{T} = E(r^2 + a^2) - aL_z, \quad (4a)$$

$$V_r = \mathcal{T}^2 - \Delta \left[ r^2 + (L_z - aE)^2 + Q \right], \quad (4b)$$

$$V_\theta = Q - \cos^2 \theta \left[ a^2 (1 - E^2) + \frac{L_z^2}{\sin^2 \theta} \right]. \quad (4c)$$

As an affine parameter, we have used Mino time which is related to the proper time  $\tau$  by [22]

$$\tau = \int r^2 + a^2 \cos^2 \theta d\lambda. \quad (5)$$

Using Mino time allows us to decouple the  $r$  and  $\theta$  motions.

We only consider bound motion [26]: the radial motion covers a range  $r_p \leq r \leq r_a$ , where the turning points are the periastris  $r_p$  and apoastris  $r_a$ . Drawing upon Keplerian orbits we parametrize the motion using

$$r = \frac{pM}{1 + e \cos \psi}, \quad (6)$$

introducing eccentricity  $e$ , (dimensionless) semilatus rectum  $p$  and relativistic anomaly  $\psi$  [27, 28]. While  $r$  oscillates between its maximum and minimum values,  $\psi$  increases secularly, increasing by  $2\pi$  across an orbit. The polar motion covers a range  $\theta_- \leq \theta \leq \pi - \theta_-$ . We also parametrize this motion in terms of an angular phase  $\chi$ , according to [29]

$$\cos \theta = \cos \theta_- \cos \chi. \quad (7)$$

While  $\psi$  and  $\chi$  are  $2\pi$  periodic they are not the canonical action-angle variables [30]; they are, however, easy to work with.

The geodesic motion can equally be described by  $\{E, L_z, Q\}$  or  $\{p, e, \theta_-\}$  [30]. Converting between them requires finding the solutions of  $V_r = 0$  and  $V_\theta = 0$ . We

employ a slightly different parameter set of  $\{p, e, \iota\}$  where we have introduced the inclination [31, 32]

$$\tan \iota = \frac{\sqrt{Q}}{L_z}. \quad (8)$$

This is  $0 \leq \iota < \pi/2$  for prograde orbits and  $\pi/2 < \iota \leq \pi$  for retrograde orbits. Equatorial orbits ( $\theta_- = \pi/2$ ) have  $\iota = 0$  or  $\pi$  and polar orbits ( $\theta_- = 0$ ) have  $\iota = \pi/2$ . While formulae exist for conversion between the different parameters, these are complicated and unisightful, so we do not reproduce them here.<sup>3</sup>

## B. Orbital resonances

The radial and polar orbital periods in Mino time are given by

$$\Lambda_r = 2 \int_{r_p}^{r_a} \frac{1}{\sqrt{V_r}} dr = \int_{-\pi}^{\pi} \frac{d\lambda}{d\psi} d\psi, \quad (9a)$$

$$\Lambda_\theta = 4 \int_{\theta_-}^{\pi/2} \frac{1}{\sqrt{V_\theta}} d\theta = \int_{-\pi}^{\pi} \frac{d\lambda}{d\chi} d\chi. \quad (9b)$$

The orbital frequencies are thus

$$\Upsilon_r = \frac{2\pi}{\Lambda_r}, \quad \Upsilon_\theta = \frac{2\pi}{\Lambda_\theta}. \quad (10)$$

The geodesic equations for coordinate time  $t$  and azimuthal angle  $\phi$  are just functions of  $r$  and  $\theta$ , hence their evolutions can be expressed as Fourier series [28]

$$\frac{dt}{d\lambda} = \sum_{k_r, k_\theta} T_{k_r, k_\theta} \exp[-i(k_r \Upsilon_r + k_\theta \Upsilon_\theta) \lambda], \quad (11a)$$

$$\frac{d\phi}{d\lambda} = \sum_{k_r, k_\theta} \Phi_{k_r, k_\theta} \exp[-i(k_r \Upsilon_r + k_\theta \Upsilon_\theta) \lambda]. \quad (11b)$$

The  $(0, 0)$  coefficients in these series give the average secular rate of increase of these quantities. We define

$$\Gamma = T_{0,0}, \quad \Upsilon_\phi = \Phi_{0,0} \quad (12)$$

to act as Mino-time frequencies. We can now convert to coordinate-time frequencies with

$$\Omega_r = \frac{\Upsilon_r}{\Gamma}, \quad \Omega_\theta = \frac{\Upsilon_\theta}{\Gamma}, \quad \Omega_\phi = \frac{\Upsilon_\phi}{\Gamma}. \quad (13)$$

Transient resonances occur when the radial and poloidal motions are commensurate, when

$$\nu = \frac{\Upsilon_r}{\Upsilon_\theta} = \frac{\Omega_r}{\Omega_\theta} = \frac{n_\theta}{n_r} \quad (14)$$

<sup>3</sup> In practice we find turning points numerically.

is the ratio of small integers. At this point, any Fourier series like those in (11b) goes from being an expansion in two frequencies to being an expansion in a single frequency [33].

For a general non-resonant orbit there is no fixed correlation between the radial and polar coordinates. After a sufficiently long time, the trajectory comes arbitrarily close to every point in the range of motion (with  $r_p \leq r \leq r_a$  and  $\theta_- \leq \theta \leq \pi - \theta_-$ ); on account of the orbital precession, the whole space is densely covered. This does not happen on resonance, as the radial and polar motions are locked together such that we can express one as a function of the other, and so the trajectory keeps cycling over the same path. The points visited are controlled by the relative phases of the  $r$  and  $\theta$  motions. To represent this, we use the  $r$  phase at the  $\theta$  turning point  $\psi_{\theta_-} = \psi(\chi = 0)$ . Varying  $\psi_{\theta_-}$  across its full range allows every point in the range of motion to be reached. Hence averaging over all values of  $\psi_{\theta_-}$  for resonant orbits is equivalent to averaging over the  $\psi$ - $\chi$  2-torus for non-resonant orbits.

One might be concerned about the nature of resonances following the inclusion of the self-force: true geodesic motion only exists at zeroth order in  $\eta$  and, while it is a good approximation over short time-scales, for small  $\eta$  there is a small disparity. The conservative piece of the self-force induces extra precession which leads to a slight shift in the orbital frequencies [34].<sup>4</sup> The dissipative piece causes the frequencies to evolve and, hence, the resonance cannot persist for multiple orbits (without some feedback coupling). In effect, we are really considering a period of time about the resonant crossing. The instantaneous orbital frequencies oscillate back and forth around their averaged values. However, there is a time span when the frequencies are consistently close to being commensurate. During this time, the trajectory appears similar to a resonant trajectory, filling only a smaller region of the parameter space. It is this time period that is of interest for transient resonances [33].

### C. Forced motion

For generic EMRIs, there are two timescales of interest: the *fast* orbital motion, related to the fundamental frequencies  $\sim 1/\Omega$ , and the *slow* inspiral, related to the change in fundamental frequencies  $\sim \Omega/\dot{\Omega}$ , where an

overdot denotes a derivative with respect to coordinate time  $t$ . These, along with the resonance timescale, are discussed more in Sec. III A. The two-timescale nature of the problem makes it ideally suited to the method of osculating elements [16]: on short timescales, we analyse the unperturbed system resulting in geodesic motion, and then the long-term evolution is described by a sequence of instantaneous geodesics.

We require, at each instant in time, that the chosen geodesic matches the true position and velocity of the particle. This amounts to a specific choice of the orbital shape parameters (for example, the set  $\{E, L_z, Q\}$  or the generalised action variables  $J_\alpha$ ) and some initial phases at  $t = t_0$  (for example, the set  $\{\psi_0, \chi_0, \phi_0\}$ ). Collectively, these are referred to as *osculating elements* and we denote them by  $I^A(t)$ , making explicit the variation with time.

Given geodesic motion in some background spacetime with Christoffel symbols  $\Gamma_{\beta\gamma}^\alpha$ , forced by some external acceleration  $f^\alpha$ , so that

$$\frac{d^2 x^\alpha}{d\tau^2} + \Gamma_{\beta\gamma}^\alpha \frac{dx^\beta}{d\tau} \frac{dx^\gamma}{d\tau} = f^\alpha, \quad (15)$$

we can calculate the evolution of the osculating elements  $\dot{I}^A$ . The specific equations for motion in Kerr are derived by Gair *et al.* [16].

### D. Self-force model

To follow the evolution of the inspiral we must have a means of prescribing the forcing acceleration. In this work we choose to work directly with the gravitational self-force, using the same post-Newtonian (PN) approximation as Flanagan and Hinderer [13]. For comparison, Flanagan, Hughes and Ruangeri [17] use a Teukolsky equation calculation of GW fluxes to account for the inspiral due to radiation reaction.

The self-force model uses the first-order PN terms of the dissipative self-force formulated in Flanagan and Hinderer [37] and the conservative force formulated in Iyer and Will [38], and Kidder [39]. Since only the first PN terms are used, this prescription can only be of limited validity in strong fields. Both pieces of the self-force are computed assuming that the spin is small: the dissipative piece contains terms to  $\mathcal{O}(a_*^2)$  and the conservative piece to  $\mathcal{O}(a_*)$ . This is less than ideal for high spins. We also find that this particular implementation of the self-force model marginally overestimates the adiabatic inspiral rate with respect to direct PN evolutions by a factor of  $\mathcal{O}(1)$ , even for systems in the weak field and with low values of the spin. While this approximate self-force is not perfect, it should serve as a guide for the behaviour of the full self-force, allowing us to assess the qualitative impact of resonances on EMRI detection.

*Add detail about why self-force model is rubbish. Comment on switching conservative piece off for population results.*

<sup>4</sup> The Kolmogorov–Arnold–Moser (KAM) theorem states that when an integrable Hamiltonian (i.e. the case for motion in Kerr) is subject to a small perturbation the form of the orbits is preserved albeit slightly deformed [35, 36]. This should ensure that, in general, there are only small shifts in the orbital frequencies. However, the KAM theory is only valid for sufficiently incommensurate orbits: close to resonance it does not apply [36]. This is a further reason why resonances merit an in-depth investigation.

## E. Adiabatic evolution

Beyond geodesic motion in the Kerr spacetime, a test particle follows an accelerated trajectory determined by (2). This may be approximated by the adiabatic prescription [20] by dropping the forcing term  $g_\alpha^{(1)}$  (and all higher-order terms) and replacing  $G_\alpha^{(1)}$  with its average over the 2-torus parametrized by  $q_r$  and  $q_\theta$ ,  $\langle G_\alpha^{(1)} \rangle_{q_r, q_\theta}$  [23]. This piece is purely dissipative and determines how the inspiral evolves due to the radiation of GWs.

To construct an adiabatic trajectory we need the 2-

torus-averaged fluxes of our osculating elements. Computing an average of a quantity over the  $\{q_r, q_\theta\}$  is trivial if it is parametrized in terms of these variables,

$$\left\langle \frac{dX}{d\lambda} \right\rangle_{q_r, q_\theta} = \frac{1}{(2\pi)^2} \int_0^{2\pi} \int_0^{2\pi} \frac{dX}{d\lambda} dq_r dq_\theta. \quad (16)$$

However, we are using  $\psi$  and  $\chi$ , as these are simpler to evolve; furthermore, we compute instantaneous co-ordinate time fluxes  $\dot{X}$ , not Mino-time fluxes. Changing variables gives an average of [23]

$$\left\langle \frac{dX}{d\lambda} \right\rangle_{q_r, q_\theta} = \frac{1}{\Lambda_r \Lambda_\theta} \int_0^{2\pi} \int_0^{2\pi} \left( \frac{d\psi}{dt} \right)^{-1} \left( \frac{d\chi}{dt} \right)^{-1} \left( \frac{dt}{d\lambda} \right)^{-2} \frac{dX}{d\lambda} d\psi d\chi \quad (17)$$

$$= \frac{1}{\Lambda_r \Lambda_\theta} \int_0^{2\pi} \int_0^{2\pi} \left( \frac{d\psi}{dt} \right)^{-1} \left( \frac{d\chi}{dt} \right)^{-1} \left( \frac{dt}{d\lambda} \right)^{-1} \dot{X} d\psi d\chi. \quad (18)$$

This average describes the Mino-time rate of change of the quantity  $X$  over an orbit. To convert to a co-ordinate flux of the averaged quantity, we simply divide by the period  $\Gamma$ , defining

$$\langle \dot{X} \rangle_{q_r, q_\theta} = \frac{1}{\Gamma} \left\langle \frac{dX}{d\lambda} \right\rangle_{q_r, q_\theta}. \quad (19)$$

It is convenient to calculate  $\Gamma$  as

$$\Gamma = \left\langle \frac{dt}{d\lambda} \right\rangle_{q_r, q_\theta}, \quad (20)$$

using (18), as this allows us to eliminate  $\Lambda_r$  and  $\Lambda_\theta$  from the calculation.<sup>5</sup> The averaged fluxes successfully describe the leading-order secular evolution of the trajectory (as illustrated in Fig. 4).

The combination of a full instantaneous evolution and an adiabatic evolution allows us to systematically study the effect of transient resonances on EMRIs over the course of an inspiral. Before approaching this problem, we first investigate the properties of the resonances themselves.

## III. PROPERTIES OF TRANSIENT RESONANCES

The first step in studying the effect of transient resonances is to locate orbital parameters for which the frequencies are commensurate. We can calculate the frequencies and so we are left with the problem of solving  $\Omega = n_r \Omega_r - n_\theta \Omega_\theta = 0$  numerically. When considering the full parameter set of  $\{p, e, \iota, a_*, \nu\}$ , it is apparent that the search for resonances becomes expensive as a consequence of the dimensionality. It is therefore useful to have a guide of where to look. In Appendix A we build a simple approximate model as a starting point for the numerical search. The resonances occur at relatively small periapses, corresponding to regions of strong-field gravity. Having located where in an inspiral we can expect to encounter a transient resonance, we must now consider its impact. In Sec. III A we determine the characteristic time-scales describing resonance, and in Sec. III B we look at the impact of passing through a resonance on the evolution of the orbit, including some numerical results.

### A. Time-scales

When analysing resonances it is useful to refer to a number of characteristic time-scales. We always use co-ordinate time  $t$  for these, as this corresponds to what is measured by an observer at infinity. Translation to Mino time can be done with an appropriate factor of  $\Gamma$ . We use the orbital period  $T$ , the evolution time-scale  $\tau_{\text{ev}}$ , the precession time-scale  $\tau_{\text{pres}}$  and the resonance time-scale  $\tau_{\text{res}}$ .

The simplest time-scales are the orbital periods  $T_r =$

<sup>5</sup> We compute these integrals using a  $300 \times 300$  grid of  $\{\psi, \chi\}$  values and employing a Newton-Cotes approximation in each dimension. The procedure requires  $\mathcal{O}(10^5)$  separate evaluations of the derivatives at each time-step of an evolution, and so is computationally expensive to perform. However, the adiabatic derivatives vary on much longer timescales than the orbital motion (see Sec. III A), and so in practice, we can interpolate.



$2\pi/\Omega_r$ ,  $T_\theta = 2\pi/\Omega_\theta$  and  $T_\phi = 2\pi/\Omega_\phi$ . These are the shortest in our set. We use  $T$  to denote a time-scale of the same order as the orbital periods.

We define the evolution time-scale as

$$\tau_{\text{ev}} = \frac{\nu}{\dot{\nu}}, \quad (21)$$

where an overdot denotes a derivative with respect to  $t$ . In general, away from resonance, we take  $\nu \equiv \Omega_r/\Omega_\theta$ . This time-scale sets the period over which there is a significant change in the frequencies. It acts as an inspiral time-scale. It is long in all cases we study,  $\tau_{\text{ev}} \sim \mathcal{O}(T/\eta)$ . It is this property which makes extreme-mass-ratio inspirals interesting, as we can follow the waveform for many cycles, accruing high signal-to-noise ratios. This is also what allows us to use the adiabatic prescription, as it means the trajectory moves slowly through different orbital parameters.

We use the precession time-scale

$$\tau_{\text{pres}}(t) = \frac{2\pi}{|\Omega(t)|}, \quad (22)$$

with  $\Omega(t) = n_r\Omega_r(t) - n_\theta\Omega_\theta(t)$ , where the frequencies are calculated instantaneously and the integers are for the resonance of interest. This time-scale becomes infinite exactly on resonance, but decreases as we get further from resonance, eventually becoming  $\mathcal{O}(T)$ . It measures the relative precession rate of the radial and polar motions and hence gives an indication of how long it takes to fill the entire  $\psi$ - $\chi$  2-torus.

We also use the resonance time-scale

$$\tau_{\text{res}} = \left[ \frac{2\pi}{|\langle \dot{\Omega}(0) \rangle_{q'}|} \right]^{1/2}. \quad (23)$$

Here  $\dot{\Omega}(0)$  is the rate of change of  $\Omega$  at resonance, which we take to be at  $t = 0$ . The instantaneous  $\dot{\Omega}$  depends upon the orbital phase and oscillates about its mean trend over an orbit. We are interested in the averaged behaviour, not the periodic modulations about this, which is why we use the time-average  $\langle \dot{\Omega} \rangle_{q'}$ ; here we use  $q'$  to represent a phase that varies over an orbit with period of order  $T$ . Close to resonance,  $\Omega(t)$  is well approximated by a first-order Taylor expansion, decreasing linearly with time; hence we make the approximation

$$\left| \langle \dot{\Omega} \rangle_{q'} \right| \simeq \left| \frac{\Omega(t)}{t} \right|. \quad (24)$$

The resonant time-scale should give an indication of the time over which we expect the effects of the resonance to be felt [33]. Consider the phase of the Mino time Fourier expansion on resonance; neglecting the constant, the resonant Fourier component has form

$$\varphi_{n_r, -n_\theta} \simeq (n_r \Upsilon_r - n_\theta \Upsilon_\theta) \lambda + (n_r \dot{\Upsilon}_r - n_\theta \dot{\Upsilon}_\theta) \lambda^2 + \dots \quad (25)$$

Typically, the first term is non-zero and this gives the familiar oscillation. On resonance, it is zero, leaving the next order term to govern the behaviour [13]. Only once we have moved far enough away from resonance for the first term to dominate the second do we recapture the non-resonant behaviour. The first term (translating from Mino time to coordinate time) sets  $\tau_{\text{pres}}$ , the second sets  $\tau_{\text{res}}$ .

Since we have argued that the effect of resonance can be thought of as a consequence of not densely covering the  $\psi$ - $\chi$  2-torus, we might expect that  $\tau_{\text{pres}}$ , as well as  $\tau_{\text{res}}$ , could be used for setting the resonance duration: the resonance ends once sufficient time has elapsed that the 2-torus could be filled. This is indeed the case. Let  $t_{\text{pres}}$  be the time taken to fill the torus, then

$$t_{\text{pres}} = \tau_{\text{pres}}(t_{\text{pres}}) \simeq \frac{2\pi}{|\langle \dot{\Omega}(0) \rangle_{q'}| t_{\text{pres}}}, \quad (26)$$

using (22) and substituting  $\Omega(t_{\text{pres}}) \simeq \langle \dot{\Omega} \rangle_{q'} t_{\text{pres}}$ . Rearranging and using (23) gives

$$t_{\text{pres}} \simeq \tau_{\text{res}}. \quad (27)$$

The two time-scales are equivalent: we preferentially use  $\tau_{\text{res}}$  to denote the resonance width. It is shorter than the inspiral time-scale, but longer than an orbital period,  $\tau_{\text{res}} \sim \mathcal{O}(\eta^{1/2} \tau_{\text{ev}}) \sim \mathcal{O}(\eta^{-1/2} T)$  [13, 16]; it therefore acts as a bridge between the two time-scales [20].

Since we shall be considering Fourier decompositions, in anticipation of future results, we also define a time-scale for the  $s$ -th resonant frequency harmonic

$$\tau_{\text{res}, s} = \left[ \frac{2\pi}{|s \langle \dot{\Omega}(0) \rangle_{q'}|} \right]^{1/2}. \quad (28)$$

This assumes that  $s$  is a non-zero integer.

## B. Resonant flux enhancement

Evolving through a resonance can lead to an enhancement (or decrement) of fluxes relative to the adiabatic prescription. After crossing the resonance region, the orbital parameters are different from those calculated from an adiabatic evolution. Flanagan and Hinderer [13] gave an expression for this deviation. If we denote the orbital parameters by  $\mathcal{I}_a = \{E, L_z, Q\}$ , then the change across resonance is

$$\Delta \mathcal{I}_a = \eta \sum_{s \neq 0} F_{a,s}^{(1)} \left[ \frac{2\pi}{|s \langle \dot{\Omega} \rangle_{q'}|} \right]^{1/2} \times \exp \left[ i \left( s \hat{\kappa}_0 + \frac{\pi}{4} \text{sgn } s \dot{\Omega} \right) \right]. \quad (29)$$

Here  $\hat{\kappa}_0$  is the orbital phase on resonance and  $F_{a,s}^{(1)}$  is the  $s$ -th harmonic of the first-order self-force on resonance, defined such that<sup>6</sup>

$$\frac{d\mathcal{I}_a}{dt} = \eta \sum_s F_{a,s}^{(1)}(\mathcal{I}) \exp(isq) + \mathcal{O}(\eta^2). \quad (30)$$

A derivation is presented in Appendix B, which contains a more comprehensive explanation of the various terms. This employs matched asymptotic expansions to track the evolution through resonance, following the approach of Kevorkian [40].

The expression for the change can be understood using our expression for the resonance width, substituting in (28),

$$\Delta\mathcal{I}_a = \eta \sum_{s \neq 0} F_{a,s}^{(1)} \tau_{\text{res},s} \exp \left[ i \left( s\hat{\kappa}_0 + \frac{\pi}{4} \text{sgn } s\dot{\Omega} \right) \right]. \quad (31)$$

Schematically, this can be understood as the magnitude of the forcing function on resonance  $\sim \eta F_{a,s}$  multiplied by the time on resonance  $\sim \tau_{\text{res},s}$  and a function that varies with the phase  $\hat{\kappa}_0$ . Averaging over all values of  $\hat{\kappa}_0$  is equivalent to averaging over all values of  $\psi_{\theta-}$ , and has the same effect as averaging over the  $\psi$ - $\chi$  2-torus; this gives an average discrepancy relative to the adiabatic evolution of

$$\langle \Delta\mathcal{I}_a \rangle_{\hat{\kappa}_0} = 0, \quad (32)$$

exactly as expected.

*Add in here some numerical results. Definitely plot showing resonant flux enhancement vs eccentricity. Probably not much else.*

We can study the predicted orbital-parameter jumps numerically by considering the long-time-average fluxes for particular (fixed) geodesics. For non-resonant geodesics, this will depend only on the orbital shape parameters, but for resonant orbits there will be an additional dependence on the initial phase difference. We consider a selection of different orbital shape parameters corresponding to low-order resonances and calculate the time-averaged fluxes for 50 different initial phases. We evolve for an integer number of cycles of both the radial and polar motions. Specifically, when considering a  $n_\theta:n_r$  resonance, we take  $T = 2\pi N n_\theta / \Omega_r = 2\pi N n_r / \Omega_\theta$  for some integer  $N$ . We have found that taking  $N = 5$  gives sufficiently accurate results. We can then estimate the jumps by taking the difference between the maximum and minimum time-averaged fluxes.

We expect nearly-circular orbits to show small flux enhancements due to the small volume of the  $r\theta$  2-torus; resonant orbits come close to every allowed point, thus approximating a non-resonant orbit. In Fig. 1, we show

the root-mean-square (over  $a$  and  $\cos\iota$ ) relative flux enhancement for the semi-latus rectum as a function of eccentricity, for a selection of low-order resonances. As expected, it is found that larger eccentricities give rise to larger resonant flux enhancements in general.

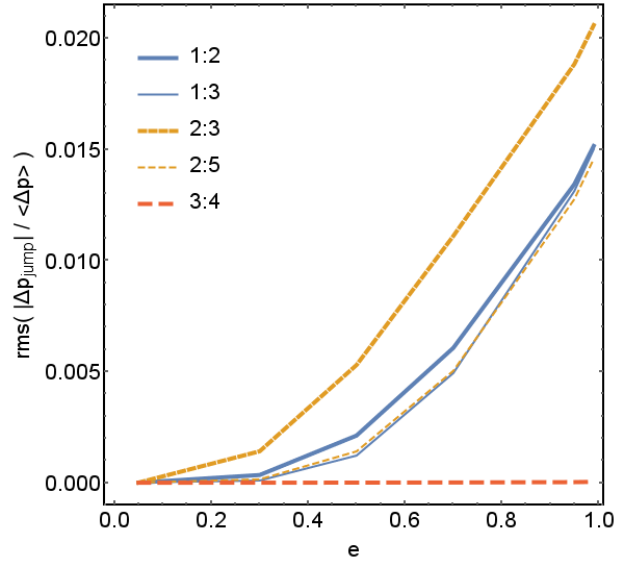


FIG. 1: Relative flux enhancements of  $p$ , as a function of  $e$ , marginalised over  $a$  and  $\cos\iota$  by taking the root-mean-square of a grid of values. Resonances with  $n_\theta = 1$  (2; 3) are coloured blue (gold; red) and use solid (short-dashed; long-dashed) lines. The 2:3 resonance has the largest relative flux enhancement.

*Is this description clear, and is it actually correct? It seems reasonable ...*

It is informative to consider the dependence on the resonance ratio  $\nu$ . Fixing the eccentricity at  $e = 0.95$  to emphasise the variation, we compute the flux enhancements for different resonance ratios, shown in Fig. 2, where we also highlight ratios arising from different values of  $n_\theta$ . We observe a clear relationship between the flux enhancement and  $\nu$  for all resonances with  $n_\theta = 1$  or 2, independent of which of those is considered. However, negligibly small flux enhancements are observed for systems with  $n_\theta = 3$  or higher. This can be explained by the quadrupolar nature of GWs. A resonant trajectory averaged over time (and consequently  $\phi$ ) takes  $n_\theta$  (possibly repeated) values of  $\theta$  at each radial turning point. Considering rings of matter at these coordinates, the dominant spherical harmonic describing the resultant mass distribution has  $l = n_\theta$  (and  $m = 0$ ). Since GWs are generated by the quadrupole moment at leading order, the most significant resonant enhancements will arise from systems with  $n_\theta = 2$ . Due to the presence of higher harmonics,  $n_\theta = 1$  systems also contribute strongly; it is perhaps more appropriate to treat 1: $x$  resonances as *de facto* 2:2 $x$  resonances, explaining the linked behaviour of the flux enhancements for  $n_\theta = 1$  and 2 systems.

*Is this bit really needed ...?*

<sup>6</sup> Since the geodesic equations decouple in Mino time rather than coordinate time, this is true only in an average sense.

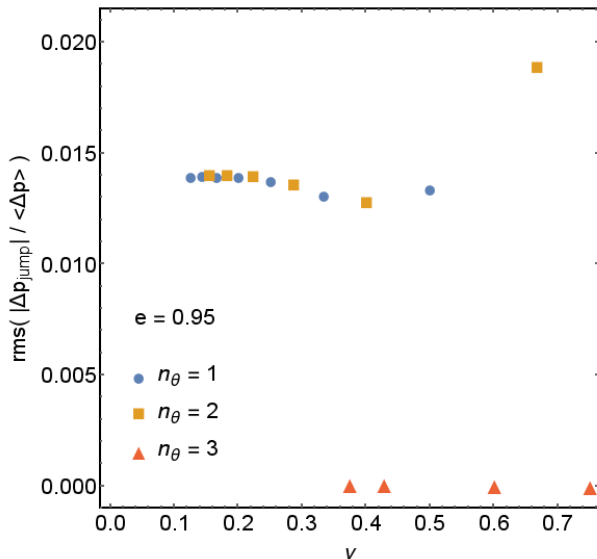


FIG. 2: Relative flux enhancements of  $p$  marginalised over  $a$  and  $\cos i$  by taking the root-mean-square. Resonances with  $n_\theta = 1$  (2; 3) are coloured blue (gold; red) and use circular (square; triangular) points.

The resonant enhancements to the fluxes of  $E$ ,  $L_z$  and  $Q$  have been calculated previously using Teukolsky-based methods for a handful of systems Flanagan, Hughes and Ruangeri [17]. They consider the 1:2, 1:3, 2:3 and 3:4 resonances for EMRIs with  $a = 0.9$ , either  $e = 0.3$  or  $0.7$ , and  $\theta_{\text{inc}} = 20^\circ$  or  $70^\circ$ . We compare our results to their published values (in their tables I–IV) in Fig. 3. There is some qualitative agreement between the two approaches: more eccentric orbits give rise to larger enhancements; and the 3:4 resonance has a negligibly small enhancement. However, for the most significant 2:3 resonance, we typically predict larger orbital parameter jumps. Our results in Sec. IV, regarding the impact of resonances on a population of EMRIs, are therefore conservative predictions, as our model over-estimates the resonance effects.

Knowing where resonances are found in parameter space, how long they last, and how big an effect they are likely to have, enables us to study and interpret the observable effects of resonances on a population of inspirals.

#### IV. ASTROPHYSICAL IMPLICATIONS

To investigate how resonances would impact real-world observations of EMRIs using GWs, we need to generate a realistic astrophysical population of EMRIs and then evolve these systems in time, including a mechanism to generate the GWs at infinity, which can then be analysed.

We discuss our chosen waveform generation scheme, giving demonstrations of its accuracy for our purposes. We then detail our procedure for generating a realistic distribution of detectable EMRIs, before turning to the

statistical effect of resonances on the population at the end of the section.

##### A. Waveform model & analysis

*Can probably shorten this section a bit.*

To generate gravitational waveforms, we employ the numerical kludge (NK) method of Babak *et al.* [41], augmented to include evolution of the positional elements. We first compute inspiral trajectories and then separately (and not necessarily consistently) calculate the GW emission sourced by a compact object moving along that trajectory. This is quicker and easier to calculate than waveforms using Teukolsky-based methods (currently the most accurate prescription available) and yet gives similar results; overlaps between Teukolsky-based and the best NK waveforms are typically 95% or higher for a variety of orbits [41, 42].

Following the NK method, we first compute the inspiral trajectory of the compact object around a central Kerr BH using the method of osculating elements detailed in Sec. II C, with the dissipative part of the post-Newtonian self-force from Sec. II D. We then map the Boyer–Lindquist coordinates to spherical polar coordinates in Minkowski, facilitating the use of a flat-spacetime waveform generation technique, the standard quadrupole formula [43].

We expect these waveforms to be sufficiently accurate for our purposes, given the inaccuracy of the self-force model being employed. It would, however, be straight-forward to adopt a different waveform generation scheme, for example by including higher-order multipole moments, should advances be made in determining the self-force.

Once we have established a waveform generation procedure, we can define a natural inner product between two waveforms,  $s(t)$  and  $h(t)$ , according to

$$(s|h) = 2 \int_0^\infty \frac{\tilde{s}(f)\tilde{h}^*(f) + \tilde{s}^*(f)\tilde{h}(f)}{S_n(f)} df, \quad (33)$$

where  $\tilde{s}(f)$  represents the Fourier transform of  $s(t)$  and similarly for  $\tilde{h}(f)$ , and  $S_n(f)$  is the one-sided noise power spectral density (PSD) [44]. We are interested in the detectability of EMRIs using future space-based GW detectors and so we use a PSD appropriate for describing the eLISA mission concept. We use the analytic approximation of Amaro-Seoane *et al.* [9]

In practice, the continuous functions  $s(t)$  and  $h(t)$  are not available, instead replaced by the time series  $s(t_i)$  and  $h(t_j)$  where  $\{t_i\}$  and  $\{t_j\}$  are equally-spaced sets of time values, but which do not necessarily have the same length or spacing. To take this into account, we project the  $h(t_j)$  onto  $\{t_i\}$  using a cubic interpolation scheme and set any values outside the domain of  $\{t_j\}$  to zero. A Planck-taper window function [45] is applied to the resulting time series to reduce unwanted spectral leakage in the Fourier



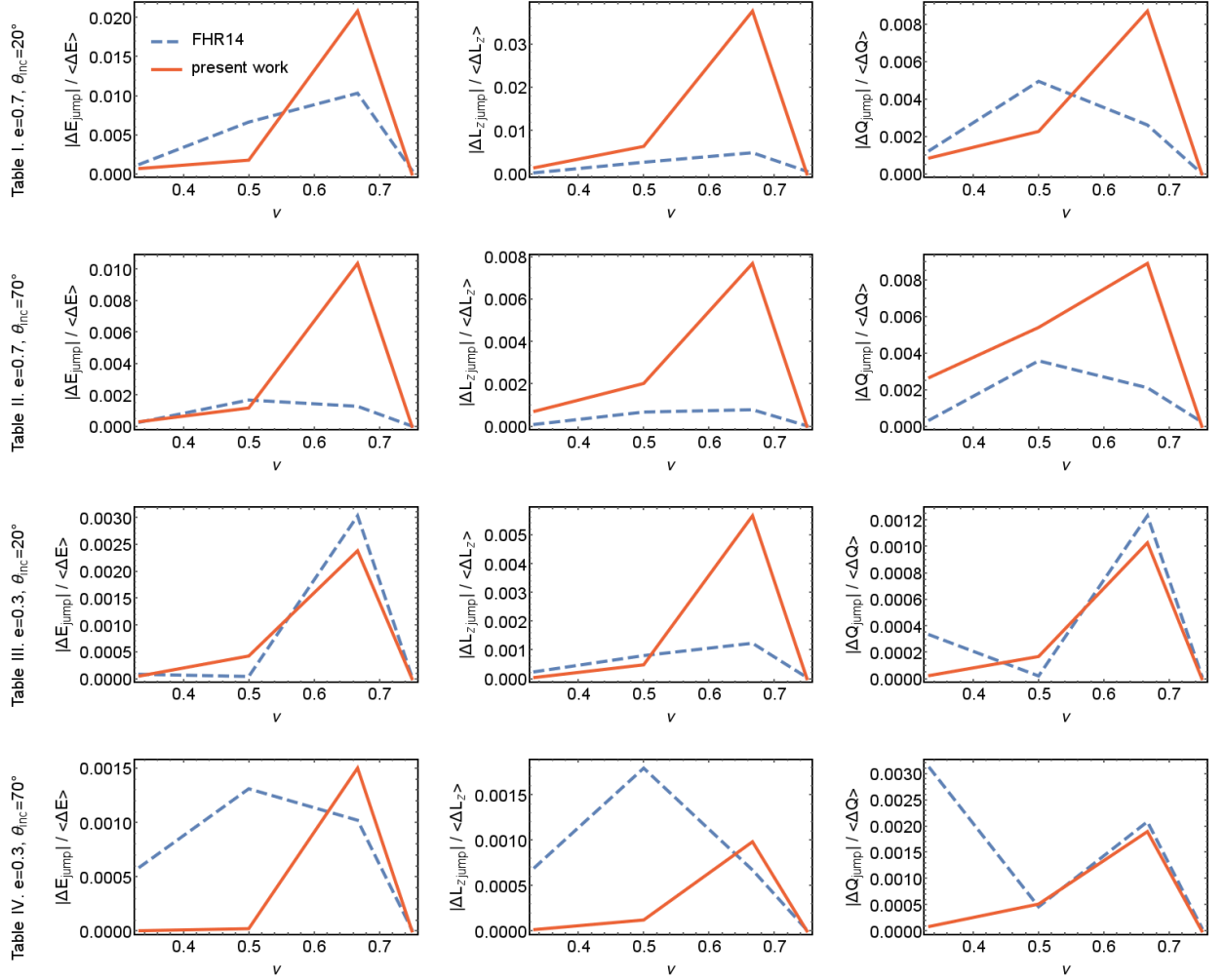


FIG. 3: Relative flux enhancements of  $E$  (left column),  $L_z$  (middle) and  $Q$  (right) for resonance ratios corresponding to the 1:3, 1:2, 2:3 and 3:4 resonances. We show results as computed here with a solid red line, and results from Flanagan, Hughes and Ruangeri (FHR14) [17] with a dashed blue line. Each row has a different eccentricity and inclination corresponding to tables I–IV in FHR14. All systems have  $a = 0.9$ .

transforms. We maximise every overlap calculation with respect to some time-offset between the models by computing the correlation between the waveforms, which can be performed cheaply using Fourier transforms.

One of the targets of pre-eLISA research is to generate a bank of waveform templates,  $h(t; \Theta^a)$  described by some set of parameters  $\Theta^a$ . Once real-world data,  $s(t)$ , has been collected, we can then search over the template bank to find the model that most closely matches the data. At the current time, with a lack of experimental data, we are interested in ensuring that the waveform templates accurately reproduce what we expect to observe in nature, without being too computationally expensive.

Ideally, we would like to use waveform templates from EMRI systems that are evolved under the entire self-force model, but these are too expensive. In practice, we are

forced to use cheaper adiabatic waveforms, but these do not include the effect of resonances. To assess the impact of this, we compare data  $s(t; \bar{\Theta}^a)$  generated using the full self-force model to templates  $h(t; \Theta^a)$  generated using the expensive 2-torus averaged self-force model (see Sec. II E).

We wish to test whether there exists some set of parameters  $\Theta^a$  such that the resulting adiabatic waveform is sufficiently similar to the full waveform. We do this by evaluating the signal-to-noise ratio (SNR) for each waveform template,

$$\rho[h] = \frac{(s|h)}{\sqrt{(h|h)}}. \quad (34)$$

If a template were to exactly match the data, it would

produce an SNR of  $\sqrt{(s|s)}$  and so the overlap

$$\mathbb{O}[h] = \frac{(s|h)}{\sqrt{(s|s)}\sqrt{(h|h)}} \quad (35)$$

provides an indication of how well-matched the template is to the data. We leave an investigation into parameter estimation biases (where the parameters of the best-matching adiabatic  $\Theta^a$  do not agree with the parameters of the system  $\bar{\Theta}^a$ ) to future work.

To demonstrate the approach, we can calculate the full evolution and the 2-torus averaged adiabatic evolution over 2 years for a set of initial parameters chosen to avoid any significant resonances. Example evolutions of the orbital parameters  $E$ ,  $L_z$  and  $Q$  are shown in Fig. 4, which shows that the adiabatic evolution closely matches the full evolution on longer inspiral timescales. The inset plots show the start of the evolution, on a timescale associated with the orbital motion of the CO; the 2-torus averaging explicitly smooths out the visible structure on this scale.

Once the trajectories have been computed using both methods of evolution, we can calculate the corresponding waveforms. The plus-polarised GW at the start and end of the evolution is shown in Fig. 5. The adiabatic waveform shows good agreement with the full waveform in both amplitude and phase. Calculating the SNR for each of the models, we find an overlap  $\mathbb{O} = 0.993$ , illustrating that adiabatic models can be used in place of the full evolution in cases where resonances are not encountered.

### B. The effect of resonances: Dephasing

The illustrative EMRI system of the previous section does not encounter a significant resonance and the adiabatic evolution provides a good match to the full evolution. We now study a system that does pass through a resonance during its 2 year evolution. Specifically, we choose the initial conditions to be the same as before but with an initial semi-latus rectum  $p = 7.85$ . This system passes through the 2:3 resonance, the effect of which is to cause a shift in the orbital parameters (and hence in the fundamental frequencies) that is not replicated by the adiabatic evolution, thus resulting in a rapid dephasing of the waveforms. Plotting the plus-polarised GWs at the start and end of the evolution, as before, demonstrates this dephasing, as shown in Fig. 6.

To highlight the dephasing more quantitatively, we calculate the shortened overlap between the two models as a function of time  $t$ , defined as the overlap obtained by including only the part of the waveform within some  $\Delta t$  of  $t$ . For our illustrative system, we choose  $\Delta t$  such that we can calculate 25 non-overlapping values of this shortened overlap. Before the resonance occurs, the adiabatic model provides a good match to the full evolution but the overlap is reduced near to the resonance and never

fully recovers afterwards. This is shown in Fig. 7, which is centered on the time at which the full evolution crosses the 2:3 resonance.

Also shown is the shortened overlap computed between the full evolution and a different adiabatic evolution that is chosen to match the full evolution at the end of the integration. In this case, we see similar behaviour as before: the adiabatic waveform has a high overlap in the region where it is constructed to match the full evolution and the boundary of that region is set by the presence of an important resonance.

### C. The effect of resonances: Loss of SNR

To be able to quantify the effect that the resonance has on an evolution, we turn to the SNR and the overlap between full and adiabatic models computed for the entire length of the observed inspiral. The dephasing means that an adiabatic evolution with the same initial conditions as a full evolution is likely to have a low overlap if a significant resonance is encountered. However, this does not necessarily mean that all adiabatic evolutions have low overlaps; we need to search for optimal adiabatic parameters, such that the overlap is maximal.

The extremely large parameter space of adiabatic waveforms, coupled with the expensive nature of our 2-torus averaging routine, renders a brute-force approach computationally impossible; it is therefore necessary to restrict the search in some way. For this preliminary investigation into the importance of resonances, we do this by focussing on a small subset of parameters that we suspect will produce a large overlap. We make the assumption that a good adiabatic model will *exactly* match the full model at some time  $t_{\text{match}}$ . This reduces the search to a one parameter family of waveforms that can easily be computed concurrently with the full evolution.

The problem of searching over adiabatic templates now reduces to the task of choosing appropriate values of  $t_{\text{match}}$ . Anticipating that resonances shall play a key role in determining the degree of waveform overlap, we choose matching times situated at  $5\tau_{\text{res}}$  after each resonance of interest, namely the low-order 2:3 and 1:2. These matching times lie in a portion of the evolution that is not affected by a resonance and so should result in a large overlap for that region of the inspiral. We also include templates that match at the start of the evolution, so that we have a model that should match the portion of the evolution before the first resonance, and at the end of the evolution, as this is often where most SNR is accumulated. In addition, we include models that match exactly on each of the resonances as these may achieve partial matching both before and after the resonance and hence perform well.

In our experience, we found that these choices were not sufficient to produce a good family of adiabatic waveforms. In particular, if an adiabatic model happened to match the full model close to the edge of the envelope

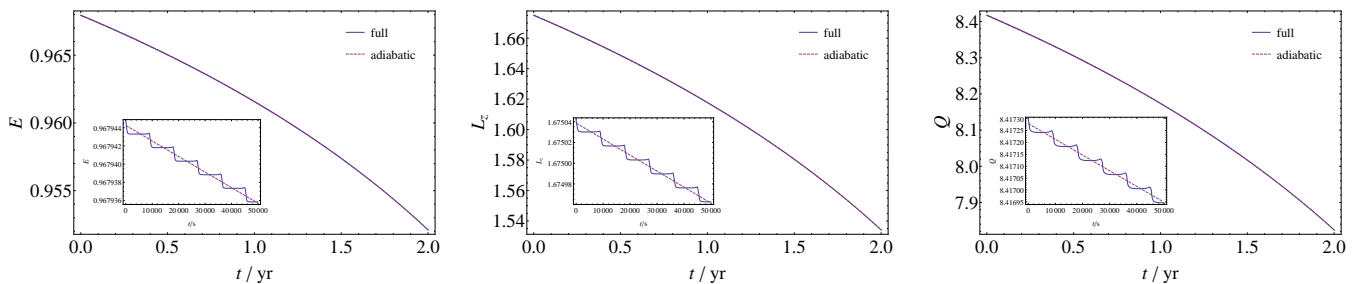


FIG. 4: The evolution of the orbital parameters  $E$  (left),  $L_z$  (center) and  $Q$  (right) under the full (solid line) and adiabatic (dashed) models for an illustrative EMRI system that does not encounter any significant resonances. The inset plots show the behaviour on short timescales, where the fast orbital oscillations can be seen. This system has  $\mu = 10M_\odot$ ,  $q = 3 \times 10^{-6}$ ,  $a_* = 0.95$ , initial semi-latus rectum  $p_0 = 7.5$ , initial eccentricity  $e_0 = 0.7$ , initial inclination  $\cos \iota_0 = 0.5$  and redshift  $z = 0.204$ .

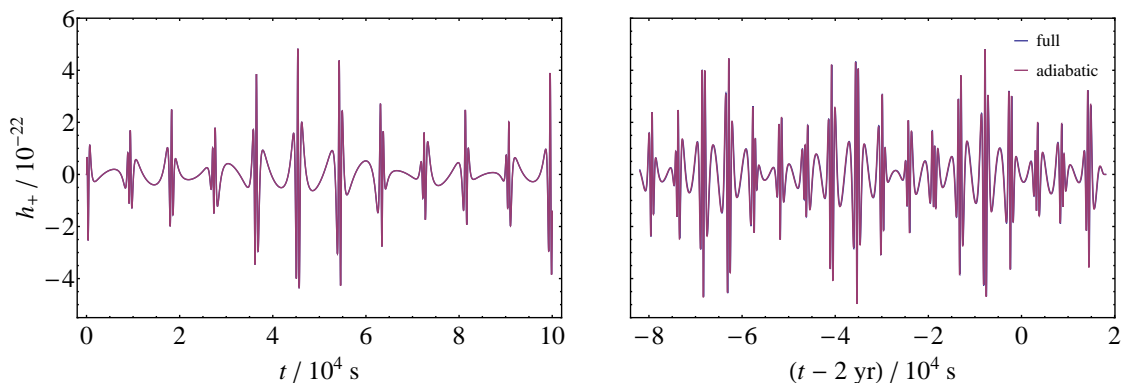


FIG. 5: The plus-polarised waveform for an illustrative EMRI system with initial semi-latus rectum  $p_0 = 7.5$ , shown for two short segments at the start and end of a 2 year evolution. The full and adiabatic models are both shown, but are indistinguishable by eye.

generated by the fast orbital evolution, then the two trajectories eventually diverged and the resulting waveform provided a poor match. We therefore adjust the values of  $t_{\text{match}}$  so that they correspond to times of apoapsis. This ensures that the adiabatic model intersects with the full model close to the centre of the envelope, as demonstrated by the inset plots in Fig. 4. As a result, we obtain much higher overlaps in general.

We have tried a more rigid system of choosing the values of  $t_{\text{match}}$ , producing an adiabatic evolution regularly at fixed intervals, but these generally perform no better than our adaptive match points and require many more adiabatic evolutions to be calculated.

This one-parameter family of adiabatic models does not explore the extrinsic parameter space nor does it consider different values of the constant intrinsic parameters (the masses of the BHs and the central BH spin). It is possible that small deviations from these true parameters give rise to better matching adiabatic models, to partially correct for the (lack of) resonance effects. Indeed, systematic biases in parameter estimation are expected when the model waveforms do not accurately reflect the data [46]. The result of these restrictions is that the maximum overlap calculated using our family is a strict lower

bound on the true maximum overlap.

For the illustrative EMRI system detailed in the previous section, we have computed the family of adiabatic models set by  $t_{\text{match}}$  and the resulting trajectories are consistent for the length of the evolution. As they cannot be easily distinguished by eye, we plot the difference (in  $E$ ,  $L_z$  and  $Q$ ) between the models and the adiabatic evolution that matches at the start, shown in Fig. 8. The jumps in the orbital parameters due to the 2:3 resonance can be clearly seen, as can the fast orbital oscillations present in the full evolution but absent in the adiabatics.

None of the adiabatic models presented here give a particularly high overlap with the full evolution, because of the effects of the resonance. The best-performing adiabatic model was that which matched at the end, giving  $\mathcal{O} = 0.677$ , while the model that matches at the start gives only  $\mathcal{O} = 0.207$ . These values can be explained qualitatively by the relative lengths of the adiabatic-like regions on either side of the resonance in the full evolution.

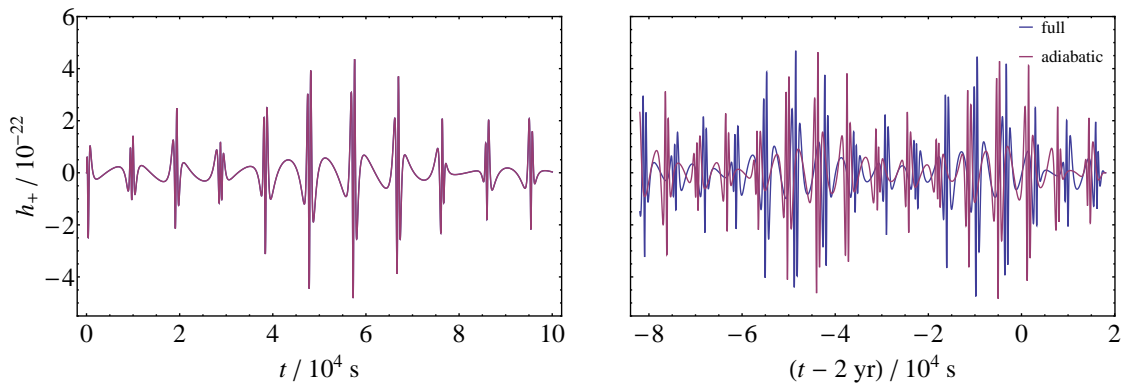


FIG. 6: The plus-polarised waveform for an illustrative EMRI system with  $p = 7.85$ , shown for two short segments at the start and end of a 2 year evolution. The full and adiabatic models are both shown; there is a significant dephasing between them by the end of the evolution.

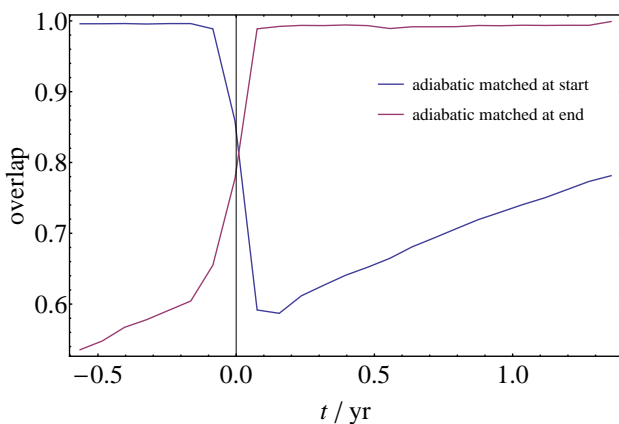


FIG. 7: The overlap computed between the full evolution and an adiabatic evolution for an illustrative EMRI system with  $p = 7.85$ , as a function of time, including only the parts of the waveforms within some  $\Delta t$  of  $t$ , arbitrarily chosen to give 25 independent (non-overlapping) calculations. The time axis is centred on the value at which the full evolution crosses the 2:3 resonance.

#### D. The effect of resonances: Jump sizes

*Update this to reflect thesis.*

As demonstrated in Fig. 8 and computed analytically in Appendix B, the full evolution undergoes a rapid change in the orbital parameters with respect to the adiabatic evolutions. To extract the magnitude of this jump from the trajectory data, we first must account for the fast orbital oscillations as well as ensuring that we include the full effect of the resonance, while minimising any changes resulting from other sources.

To achieve this, we isolate spans of data away from the resonance; specifically, looking at data that lies within five and ten resonance timescales away. For both the pre- and post-resonance datasets, we compute  $\Delta\mathcal{I} \equiv \mathcal{I}_{\text{full}} - \mathcal{I}_{\text{ad}}[t_{\text{match}} = t_{\text{res}}]$  for each of the orbital param-

eters. We then identify the most horizontal straight lines that bound the data, which give an approximation to the behaviour of the fast orbital oscillations. The resulting data and bounding lines are shown for our illustrative system in Fig. 9.

To estimate the size of the jump  $\Delta\mathcal{I}_{\text{jump}}$ , we extrapolate the bounding lines to the resonance time and calculate the difference between the pre- and post-resonance values, quoting the final result as the average of that obtained using the upper and lower limits. This allows us to take into account any linear drift in  $\Delta\mathcal{I}$  that can occur over the resonance timescale due to the inaccuracy of the adiabatic approximation. For typical systems, this numerically computed jump appears to well describe the resonance, as shown by the red dotted line in Fig. 9.

The absolute size of the resonance jump is often not particularly useful, especially when comparing different systems. Instead, we can express the resonance jump as a fraction of the adiabatic change expected across the resonance. For the orbital parameter  $\mathcal{I}$ ,

$$\frac{\Delta\mathcal{I}_{\text{jump}}}{\mathcal{I}_{\text{ad}}(t > t_{\text{res}}) - \mathcal{I}_{\text{ad}}(t < t_{\text{res}})} = \frac{\Delta\mathcal{I}_{\text{jump}}}{\dot{\mathcal{I}}_{\text{ad}}(t_{\text{res}})\tau_{\text{res}}}. \quad (36)$$

The resonance jump depends sensitively on the relative phase of radial and poloidal motions. It is therefore instructive to study the resonance problem using an ensemble of systems differing only in the initial value of the radial phase  $\psi$ , which we do for our illustrative system parameters. Choosing random values for  $\psi$  corresponds to random values of the orbital phase on resonance  $\hat{\kappa}_0$ , which should map out the full range of resonance jumps for these particular orbital shape parameters, according to (31).

Given our computed resonance jumps for all of the orbital parameters, we extract a single phase parameter  $q$  for each system that specifies the magnitude of each jump. We expect such a phase parameter to be linearly offset from  $\hat{\kappa}_0$ . The resonance jumps are sinusoidal with respect to  $q$ , as shown by the fits in Fig. 10, lending sup-

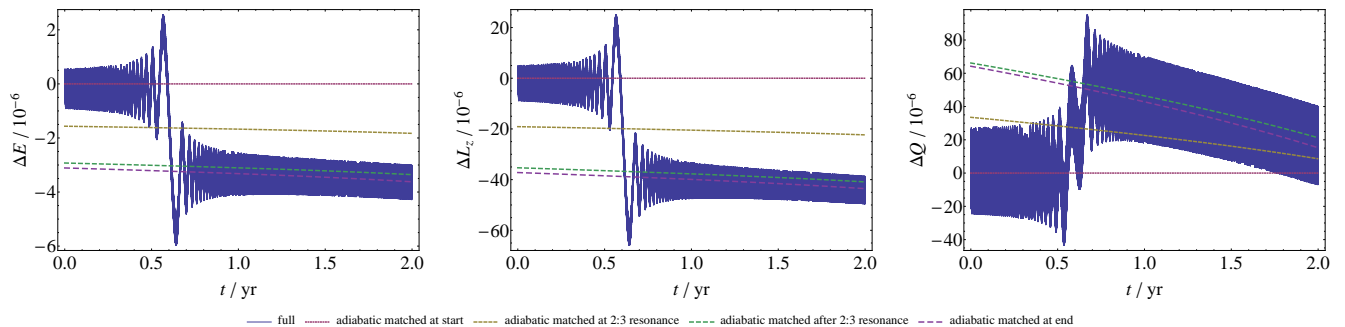


FIG. 8: The differences in orbital parameters  $E$  (left),  $L_z$  (center) and  $Q$  (right) between each evolution scheme and the adiabatic model that matches at the start. The solid line shows the full evolution and the dashed lines show the different adiabatic evolutions, which match the full evolution at different times throughout the inspiral (numbers in parentheses give the overlap with the full evolution): at the start (0.207), at the 2:3 resonance (0.432), after the 2:3 resonance (0.258) and at the end (0.677).

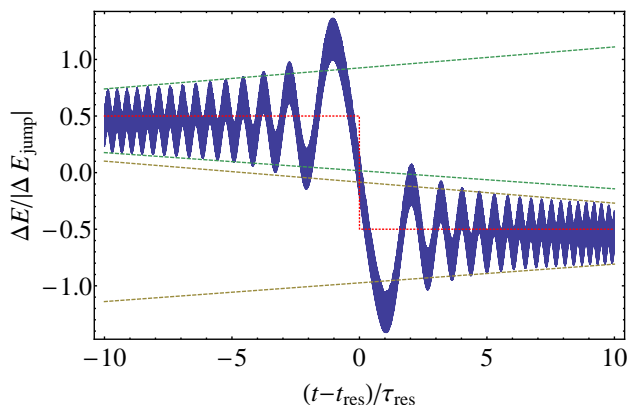


FIG. 9: The difference in energy between the instantaneous model and adiabatic model that matches at the 2:3 resonance, scaled by the magnitude of the 2:3 resonance jump. The dashed green (yellow) lines show the bounding fits to the data before (after) the resonance, used to numerically estimate the size of the jump. The dotted red line indicates the computed size of the jump. The time axis is centred on the 2:3 resonance and is scaled by the appropriate resonance timescale.

port to (31) and giving us confidence in our numerical jump calculations. The jumps in  $E$  and  $L_z$  are approximately in phase, but those in  $Q$  are found to be offset; this means that for every value of  $q$ , there is always a resonance jump in at least one parameter. We can also compute the jumps in the fundamental frequencies for each system (shown as dashed lines in Fig. 10).

For each system, we compute the overlap between the full evolution and the family of adiabatics given by our set of match times  $t_{\text{match}}$  described in the previous section. The largest overlap in each case, plotted in Fig. 11, appears to be roughly independent of the value of  $q$  and hence with the relative sizes of the orbital parameter jumps.

The best performing adiabatic for the majority of our systems matched at the end of the inspiral. We can there-

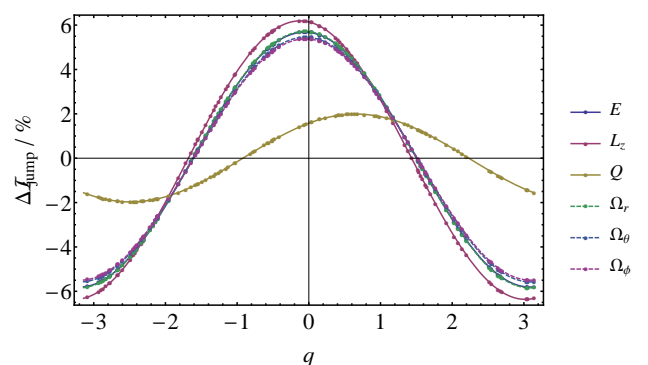


FIG. 10: The magnitude of the resonance jump for our illustrative system as a function of the extracted phase parameter  $q$ . The jump is expressed as a percentage of the adiabatic change in each parameter, given by (36). The individual jumps as well as a sinusoidal fit are plotted for the three orbital shape parameters (solid lines) and the three orbital frequencies (dotted).

fore estimate the value of the overlap by assuming that the adiabatic waveforms recover the entire SNR in the region post-resonance, but none at all in the region pre-resonance. We expect the overlap to scale with the fraction of time spent post-resonance, the value of which is demonstrated by the red line in Fig. 11. There is not an exact equivalence because of the frequency-dependent noise of eLISA; cycles near the end of the inspiral accumulate proportionally more SNR at a frequency closer to the minimum of the eLISA noise curve.

Systems with  $|q| \approx \pi/2$  (corresponding to small jumps in  $E$  and  $L_z$ ) have higher than average overlaps due to additional accumulation in the pre-resonance region. The adiabatic models of these systems dephase more slowly, but still do not produce very high overlaps due to the jump in  $Q$ . A small fraction of systems have a lower overlap than expected, at around 0.5. This is due to a sub-optimal choice of the matching times; making small



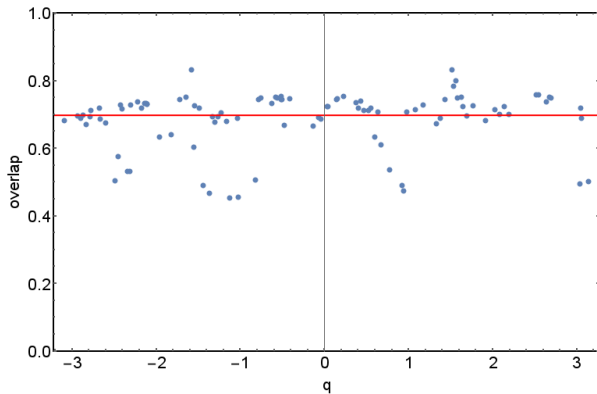


FIG. 11: The overlap between the full and adiabatic evolutions, maximised over the family of generated adiabatics, as a function of the extracted phase parameter  $q$ . Each dot represents a system with our illustrative parameters and a random choice of the initial radial phase. The red line indicates the expected overlap assuming that the waveforms match exactly post-resonance, but have zero overlap pre-resonance.

adjustments to  $t_{\text{match}}$  can lead to higher overlaps, but the exact adjustments required are difficult to predict in advance.

### E. Sample EMRI population

*Basically summarise the GOAT population. Maybe include event rate estimates in appendix??*

Strong resonances can limit our ability to recover SNR from waveforms using adiabatic templates; they partition the inspiral, splitting up the total SNR into different adiabatic regions, which may be individually undetectable. In order to assess the impact of this on future GW missions, we need to analyse the waveforms from a population of detectable EMRIs.

We generate a representative EMRI population by making reasonable assumptions about the distributions of the 14 parameters in the analytic kludge model of Barack and Cutler [47]. The EMRI event rate is dominated by the inspiral of heavier BHs due to the larger observational volume in comparison to that for white dwarfs and neutron stars [48]. We therefore take the mass of the compact object to be  $\mu = 10M_{\odot}$ , corresponding to a typical mass for stellar BHs.

We take the central object to be a typical supermassive BH at the centre of a galaxy; we construct an appropriate distribution by breaking the EMRI event rate into two pieces: the ‘intrinsic’ event rate  $\mathcal{R}$ , i.e. the number of inspiral events per unit time for any given galaxy; and the comoving number density of SMBHs in the Universe, which is the same as that of galaxies if we assume all galaxies host a single SMBH. We are interested in galaxies that possess a SMBH with a mass in the range  $(10^4 - 10^7)M_{\odot}$ , as these give rise to EMRIs in the frequency band of space-based GW detectors. In principle,

$\mathcal{R}$  will depend on the exact composition of the population of compact objects around each SMBH, the stellar density profile for each component, and the mass and spin of each SMBH. All of these properties are highly uncertain, even for our own galaxy.

Despite the difficulties, simple estimates of  $\mathcal{R}$  have been carried out using Monte Carlo methods to count the number of stars from isothermal distributions that spiral in to a SMBH without plunging. The result is a scaling law for each species of compact object of the form

$$\mathcal{R}(M) = \mathcal{R}_0 \left( \frac{M}{M_0} \right)^{\alpha}, \quad (37)$$

where  $M$  is the mass of the SMBH and  $M_0 = 3 \times 10^6 M_{\odot}$  is some fiducial mass. Hopman [49] finds that  $\alpha = \{-0.15, -0.25, -0.25\}$  for BHs, NSs and WDs, with respective event rates  $\mathcal{R}_0 = \{400, 7, 20\} \text{ Gyr}^{-1}$  for each component. This neglects the effects of resonant relaxation, ignores the spin of the SMBH, and assumes that the  $M$ - $\sigma$  relation holds for all SMBH masses. Each of these is likely to significantly impact the event rate, but (37) can still be used as a rough guide to the expected number of events.

Amaro-Seoane and Preto [50] studied the effects of mass segregation on the intrinsic EMRI event rate, using direct-summation  $N$ -body simulations to calibrate a Fokker-Planck description for the bulk properties of the stellar distribution. They found a better fit for the power law spectral index for BHs of  $\alpha = -0.19$ .

The comoving number density of galaxies is challenging to estimate due to local structure in the Universe, the evolution of that structure, and properties of the SMBHs themselves. We simplify the problem by assuming a homogeneous distribution that does not evolve with redshift, which is reasonable for the typical scales considered by GW detectors. We also neglect correlations between the SMBH mass and spin, and impose a power law scaling relation for the comoving number density

$$\frac{dn}{d \ln M}(M) = n_0 \left( \frac{M}{M_0} \right)^{\beta}. \quad (38)$$

There is significant uncertainty in the SMBH mass function, but this simple functional form is found to be in good agreement with observations from the Sloan Digital Sky Survey for the mass range of interest; it is sufficient to set  $\beta = 0$  and  $n_0 = 0.002 \text{ Mpc}^{-3}$  for SMBHs with  $M < \mathcal{O}(10^7 M_{\odot})$  [51, 52].

The mass of the SMBH is then sampled from a power-law with a probability distribution function (pdf)  $f(M) \propto M^{\alpha+\beta-1}$ . We sample the dimensionless spin  $a_*$  uniformly between its limiting values, 0 and 1. The direction of the spin of the central BH, the direction of the angular momentum of the orbit and the direction of the source on the sky are all chosen uniformly on the sphere. The angles specifying the location of pericenter and the compact object around the orbit are distributed uniformly between 0 and  $2\pi$ .

We assume a standard cosmology with  $\Omega_\Lambda = 0.7$ ,  $\Omega_m = 0.3$  and  $H_0 = 70 \text{ kms}^{-1} \text{ Mpc}^{-1}$ , and sample the redshift of the source uniformly from comoving volume, up to a maximum of  $z_{\text{max}} = 1.5$ . We don't expect the exact details of the cosmology to significantly alter our results and our choice of  $z_{\text{max}}$  is justified *post hoc*.

The eccentricity distribution is more complicated. Eccentricities for EMRIs are uncertain, and depend strongly on the formation scenario being considered. Here, we adopt a fit to a distribution computed using Monte Carlo

simulations by Hopman and Alexander [53], who model the scattering process of compact objects onto inspiral orbits around a  $3 \times 10^6 M_\odot$  Schwarzschild BH. We assume this can be extended to provide a rough estimate of the distribution around BHs of other masses and spins. At the point in the inspiral when the orbital period takes a fiducial value  $\nu_0 = 10^4 \text{ s}$ , we find that the Monte Carlo eccentricity pdf is well-described by a power-law with an exponential cutoff

$$f(e; e_m, e_p, b) \propto \begin{cases} (e_m - e)^{b(e_m - e_p)} \exp\{b(e - e_m)\}, & 0 \leq e \leq e_m \\ 0, & \text{otherwise} \end{cases} \quad (39)$$

where  $e_m = 0.81$  is the maximum observed eccentricity,  $e_p = 0.69$  is the peak of the distribution, and  $b = 11$  is the exponential index.

We are interested in EMRI systems close to plunge, as it is here where the GW amplitude is largest. To create our EMRI population, we therefore sample the eccentricity from the distribution given by (39), set the orbital period equal to the fiducial value of  $10^4 \text{ s}$ , and evolve the system using the AK prescription up until the last stable orbit (LSO).<sup>7</sup> Each of these systems is then evolved backwards for some time  $t_{\text{insp}}$ , chosen uniformly from the range  $[0, 2]$  years, and the expected gravitational waveforms are calculated using the AK formalism.

The size of the required population can be estimated by evaluating an integral of the form [54]

$$N_{\text{EMRI}} = \int_{z=0}^{z_{\text{max}}} \int_{M=M_{\text{min}}}^{M_{\text{max}}} \mathcal{RT} \frac{dn}{d \ln M} \frac{dV_c}{dz} d \ln M dz, \quad (40)$$

where  $V_c(z)$  is the comoving volume at redshift  $z$ . For a mission lifetime of 2 years, the integral gives a total of 6333 EMRI events. This is a lower bound for  $N_{\text{EMRI}}$  as we are neglecting EMRIs that merge outside the observation window but nevertheless accumulate sufficient SNR during this time to be observable.

A given EMRI is classified as observable if its SNR exceeds some threshold value  $\text{SNR}_{\text{thres}}$ . Calculating SNRs from the generated AK waveforms, assuming 6 laser links and using the eLISA noise PSD, we find 513 detectable events, assuming an SNR threshold of 15. The parameter distributions for the mass and spin of the SMBH, the orbital shape parameters, the redshift of the source,

and the length of the observation  $t_{\text{insp}}$  are shown in Fig. 12, to be contrasted with the distributions of the 5820 systems with an SNR less than 15, which are also shown.

We note that eccentric prograde orbits around SMBHs with larger spins tend to produce larger SNRs, due to the fact that the periaapse in such systems can get much closer to the SMBH, and so the compact object experiences the strongest gravitational fields. This effect also causes the detectable EMRIs to have smaller values of  $p$  at plunge, as observed in the distributions. Systems at higher redshifts start to become undetectable because the amplitude of the signal scales inversely proportional to the luminosity distance to the source, and by  $z = 1.5$ , the distribution of detectable EMRIs with eLISA has essentially vanished. The mass distribution for detectable EMRIs is peaked such that the typical GW frequency occurs at the base of the eLISA noise PSD.

EMRI systems within our population tend to have small eccentricities at plunge due to the circularising effect of GWs: 85% of detectable systems have  $e < 0.1$ , with a mean value of 0.05 and a maximum of 0.4. In Sec. IIIB, we found a strong eccentricity dependence on the magnitude of the resonant flux enhancements. We therefore expect typical resonant jumps in these astrophysical systems to be much less than 1%, and so the resultant dephasing may be relatively weak. We now analyse these 513 systems using our full and adiabatic self-force models.

## F. Loss of signal-to-noise ratio

After computing the SNRs of our NK waveforms for each of the 513 systems, we can compare the values to those obtained using the AK formalism. The different approximation schemes are expected to produce different results, but they should be broadly similar. In Fig. 13, we plot the ratio of the new SNR to the AK SNR, as a function of the mass ratio. We observe a clear trend,

<sup>7</sup> The LSO is determined numerically by calculating the roots of  $R(r) = 0$ , which we denote in ascending order by  $r_4 \leq r_3 \leq r_p \leq r_a$ , and stopping the evolution when  $r_3 = r_p$ , which designates the orbit as marginally stable.

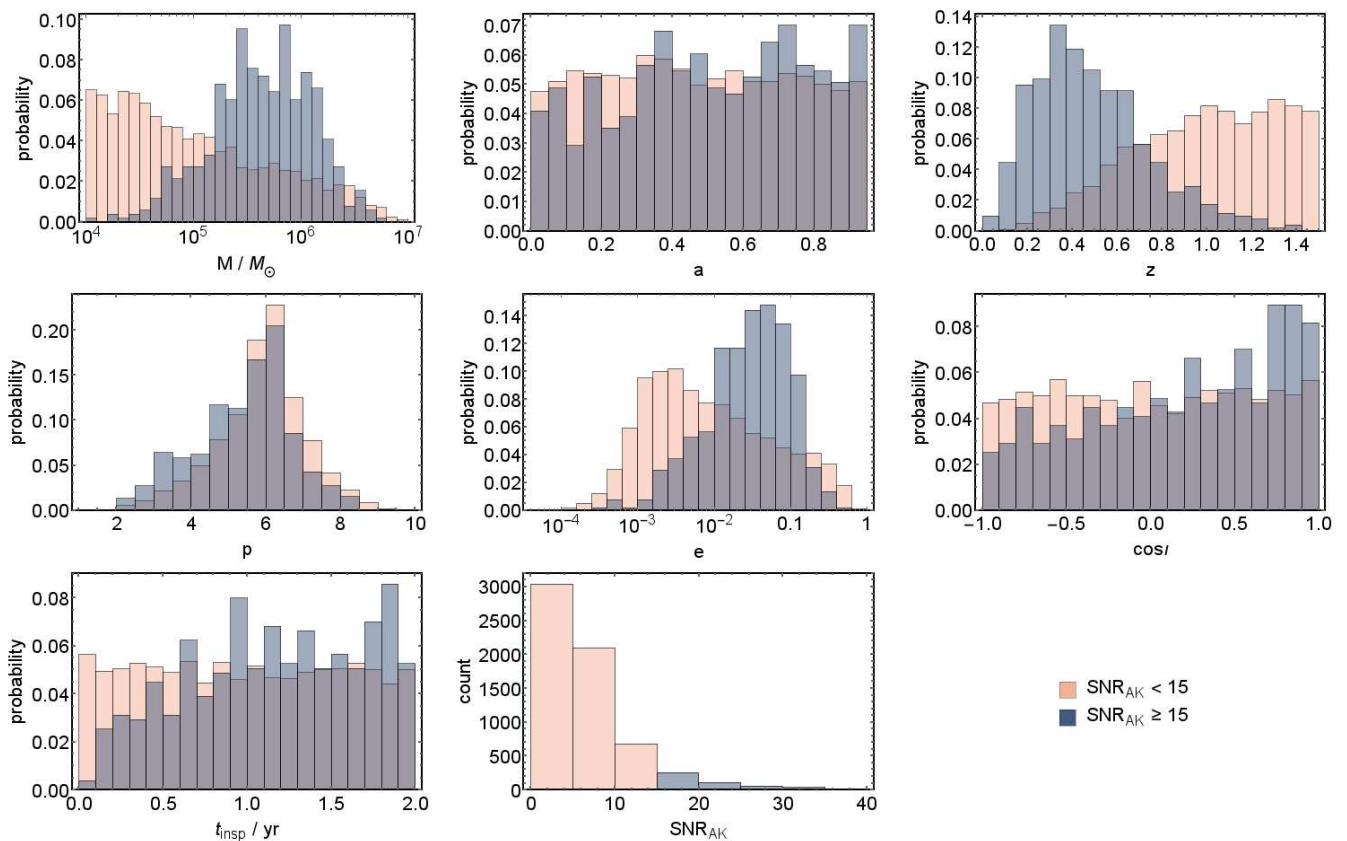


FIG. 12: The parameter distributions at plunge for our detectable EMRI systems (dark blue), alongside those of the undetectable systems (light pink). In each case, the y-axis values are the probability of a system being found in a particular bin, given that they are either detectable or undetectable. The exception to this is in the final plot for the SNR, where we show the number of systems in each bin. The SNRs quoted here are calculated using the AK model.

with systems closest to equal mass performing roughly as expected, but with the most extreme systems giving significantly lower SNRs.

This is a consequence of the PN self-force model we are using, which we have found overestimates the inspiral rate for EMRIs. Detectable systems with larger mass ratios (closer to equal mass) plunge at higher frequencies, and so during the 2 year observation window, they evolve within the bucket of the eLISA noise curve. Increasing the rate of evolution then does not significantly change the recovered SNR since we are still sensitive to all parts of the waveform. At smaller mass ratios, the systems evolve more slowly, from lower plunge frequencies. An increased evolution rate can shift the EMRI to outside the sensitive region of the detector, thus giving a much lower SNR.

Nevertheless, we may still study the effect of resonances, by comparing the maximum adiabatic SNR to the full SNR computed using the NK waveforms. The resulting overlap is still indicative of the effect of resonances on the population of systems.

We have calculated the longest period of time,  $t_{\text{ad}}$ , during each inspiral, in which neither the 1:2 nor the 2:3 resonance occurs. From the results of Sec. ??, we expect

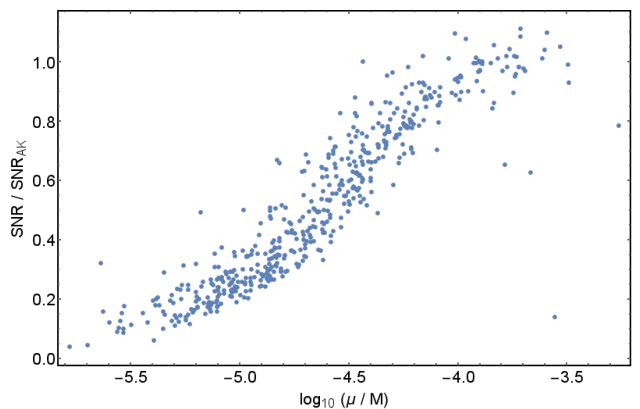


FIG. 13: The ratio of SNRs as computed with waveforms generated using the NK (adopting our PN self-force model) and AK formalisms, as a function of (the base-10 logarithm of) the mass ratio. Each system has an AK SNR greater than 15, using the eLISA detector with 6 laser links.

the recovered overlap to be approximately given by the proportion of time spent in a resonance-free region, that is  $t_{\text{ad}}/t_{\text{insp}}$ . In Fig. 14, we plot the maximum overlap

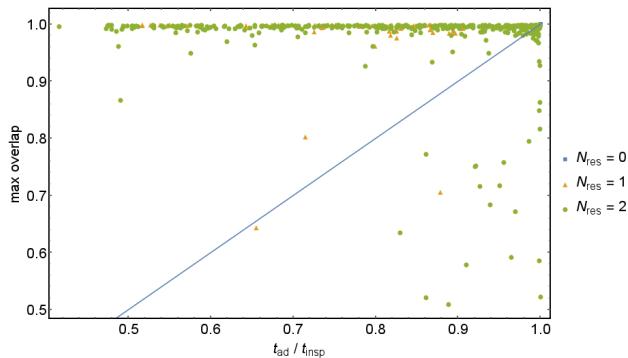


FIG. 14: The maximum overlap for 513 detectable EMRI systems obtained by comparing the instantaneous evolution with each of the adiabatic models in our one-parameter family. Each system encounters either 0 (blue squares), 1 (gold triangles) or 2 (green circles) resonances during the observation window  $t_{\text{insp}}$ . The overlap is plotted against the largest time spent by the inspiral without encountering any resonances  $t_{\text{ad}}$ , normalised by  $t_{\text{insp}}$ . The solid line corresponds to the expected value if the 1:2 and 2:3 resonances cause significant waveform dephasing.

between the instantaneous and adiabatic models against this ratio, highlighting the number of resonances,  $N_{\text{res}}$ , each system encounters. In the majority of cases, there is no significant impact on the recovered overlap using adiabatic models.

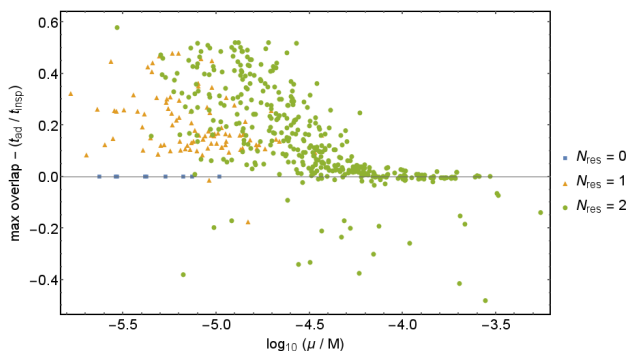


FIG. 15: The difference between the maximum overlap and the expected value  $t_{\text{ad}}/t_{\text{insp}}$ , as a function of (the base-10 logarithm of) the mass ratio.

We can better understand the overlap distribution from Fig. 14 by considering the behaviour with the mass ratio. We do this in Fig. 15, plotting the difference between the computed maximum overlap and the value expected should resonances be important. A small proportion of systems have overlaps below the expected value (approximately 4% have values less than  $-0.05$ ). This might be caused by higher-order resonances disrupting the evolution, in which case  $t_{\text{ad}}$  should be smaller and the systems would lie on the expectation line. Alternatively, the low-order resonances might be long-lived, explaining why the recovered overlap is smaller than expected. However, a more likely explanation is that larger

adiabatic overlaps are possible with models that we have not considered here (either with different values of  $t_{\text{match}}$  or outside our one-parameter family altogether).

Roughly 30% of the systems lie within 0.05 of the expected value. However, the vast majority of these are not significantly disrupted by resonances, and produce overlaps approaching unity. For the smallest mass ratios, the inspiral rate is slow, and so the systems do not encounter either the 1:2 or 2:3 resonances during their lifetime. Meanwhile for the largest mass ratios, the EMRIs encounter both resonances very close to plunge. In each case, there is a long resonance-free region, allowing a high overlap to be recovered.

The remaining 66% of systems have overlaps above the level expected if resonances were to play an important role. These occur at low and intermediate values of the mass ratio, where the inspiral rate is slow enough that the low-order resonances are encountered in the middle of the observation window, and the resulting value of  $t_{\text{ad}}$  is small. For these EMRIs, resonances are not as important as expected, which is likely due to the low eccentricities of our population leading to small (and in most cases, negligible) resonant flux enhancements.

Even if we assume that all overlap reductions are due to resonances (instead of due to our adiabatic family not being extensive enough) the overall effect on the population is not significant. To illustrate this, we plot the AK SNRs in Fig. 16, multiplied by the maximum recovered overlap to take into account the resonance behaviour. The total number of detectable systems using a threshold SNR of 15 decreases from 513 to 492. If we increase the threshold, the fractional reduction in the number of detectable systems gets even smaller. We therefore conclude that resonances do not cause sufficient waveform dephasing across a population of EMRIs for the detection rate to be appreciably diminished.

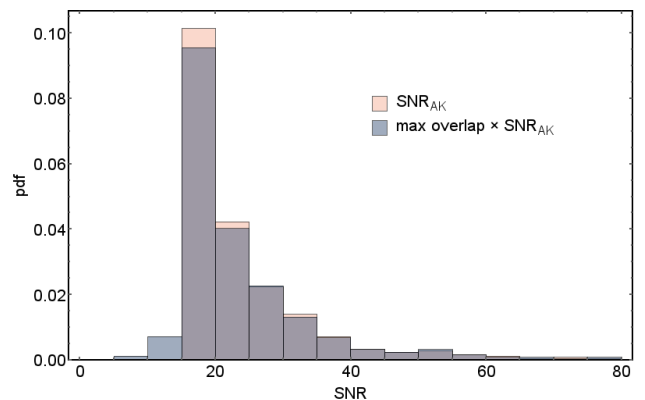


FIG. 16: Histogram showing the probability distribution function for the detectable EMRI SNRs, as calculated using the AK formalism (light pink) and modified by the maximum adiabatic overlap (dark blue).



## V. CONCLUDING REMARKS

### *Need to reconclude*

Transient resonances in EMRIs are an important consideration in waveform modelling due to the high proportion of expected systems encountering a low-order resonance in the later stages of inspiral. We have presented an evolution scheme appropriate for studying the effects of resonances on inspirals, which has been applied to an astrophysically realistic population. The location and duration of resonances, as well as their effect on orbital parameters, can all be calculated.

Amongst a population of sources, unmodelled resonances could diminish detection prospects. However, due to the low eccentricity of detectable sources, the overall effect on SNR recovery is small; it is therefore likely to be sufficient to use adiabatic models to detect EMRIs. An unresolved question here is how using these adiabatic models would affect parameter estimation: systematic biases may be introduced if we neglect the presence of important resonances. One method of providing an answer to this problem is to perform an MCMC parameter estimation study using our adiabatic waveforms as templates; we leave this to future work.

High eccentricity EMRIs may be possible, in which case transient resonances will play an important role in their detectability; systems that undergo a jump of a few percent dephase very rapidly from the adiabatic approximation. In such scenarios, adiabatic models can still be used, but there must be sufficient SNR in each non-resonant region that they can be detected as individual sources and then identified as arising from the same inspiral. If this is not possible, (31) can be used to join together different adiabatic models, if the phase on resonance and the magnitude of the self-force can be predicted sufficiently accurately. Alternatively, the jump  $\Delta Z_{\text{jump}}$  for each orbital parameter could be included as a free parameter in the template space, and then searched over. Such hybrid models merit further study as relatively simple ways of incorporating resonance effects into adiabatic models.

This work is highly dependent on the chosen self-force model, and so the results should be taken as qualitative estimates, given the unsuitability of a PN self-force to the problem of fast motion near to highly-spinning BHs. In the future, with a more accurate self-force model, more exact quantitative results can be derived.

### Acknowledgments

The authors extend our sincere gratitude to Éanna Flanagan and Tanja Hinderer for providing their PN self-force code, without which this work would not be possible. We also wish to thank Tanja Hinderer, Jeandrew Brink, Maarten van de Meent and Leor Barack for useful conversations. RHC is supported by STFC; CPLB thanks STFC and the Cambridge Philosophical Society;

PC was supported by a Marie Curie Fellowship, and JRG is supported by the Royal Society.

## Appendix A: Location of resonances

We can find the location of resonances by numerically solving  $\Omega = n_r \Omega_r - n_\theta \Omega_\theta = 0$ . Fig. 17 shows the semilatus rectum, eccentricity and (cosine of the) inclination angle of the  $\nu = 2/5$  resonance surface for a BH of spin  $a_* = 0.95$ . This is almost planar, inspiring us to look for

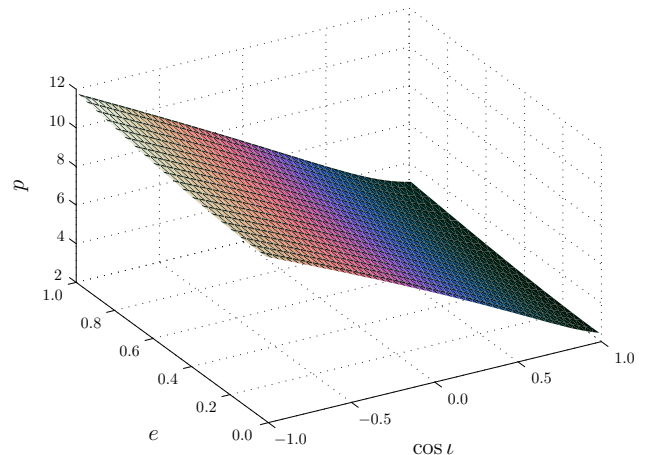


FIG. 17: Location of the  $2/5$  resonance surface for an  $a_* = 0.95$  BH in terms of orbital semilatus rectum  $p$ , eccentricity  $e$  and inclination  $i$ .

a simple description that can help guide our search for resonance locations. Brink, Geyer and Hinderer [55] provide series expansions for the location of resonances in the limit of equatorial orbits for small spin and eccentricity. We do not follow this approach of trying to find analytic expressions for the resonance surface. The expressions become complicated when venturing away from limiting cases. Instead, we build an approximate phenomenological model and fit this to the resonance plane. This should be useful for designating the region in which resonance could be expected. To locate them precisely, it is necessary to solve  $\Omega = 0$  numerically; the approximate model gives a suitable starting point.

The resonant semilatus rectum for any particular spin and resonance ratio can be well approximated as

$$p(e, i; a_*, \nu) \simeq A \frac{1 + Be + D \cos i}{1 - C \exp(e)}. \quad (\text{A1})$$

The coefficients  $\{A, B, C, D\}$  depend upon the spin and the particular resonance; they can be approximated as

$$A(a_*, \nu) \simeq a_0 \frac{1 + a_1 \nu - a_2 \nu^2 - a_3 \nu a_*^2}{1 + a_4 \nu - (1 + a_4) \nu^2}, \quad (\text{A2})$$

$$B(a_*, \nu) \simeq b_0 (1 - b_1 \nu) \exp(-b_2 \nu) (1 - b_3 a_*), \quad (\text{A3})$$

$$C(a_*, \nu) \simeq c_0, \quad (\text{A4})$$

$$D(a_*, \nu) \simeq d_0 [1 - \exp(a_*)] [1 - d_1 \exp(\nu)]. \quad (\text{A5})$$



This gives us a total of 12 parameters for our fit. Whilst this may sound large, if we were fitting an expansion to quadratic order in any combination of  $\{e, \iota, a_*, \nu\}$  we would have 15 parameters.<sup>8</sup> Our optimised parameters are

$$\begin{aligned} a_0 &= 5.9854, & a_1 &= 3.4116, & a_2 &= 0.9253, \\ a_3 &= 0.1959, & a_4 &= 4.8846, & b_0 &= 0.7692, \\ b_1 &= 1.4752, & b_2 &= 1.4861, & b_3 &= 0.5974, \\ c_0 &= 0.02332, & d_0 &= 0.7968, & d_1 &= 0.3115. \end{aligned} \quad (\text{A6})$$

These were fitted for all possible resonances with  $n_r = 2-7$  as well as the  $9 : 10$ ,  $19 : 20$ ,  $49 : 50$  and  $99 : 100$  resonances; with MBH spins of  $a_* = 0.01-0.999$ ; for orbits with eccentricities  $e = 0.01-0.99$ , and inclinations  $\cos \iota = -0.999999-0.999999$ .

Using this approximation, the maximum error in  $p$  for a given  $a_*$  and  $\nu$  is typically  $\sim 10\%$  and less than 1 in absolute terms. The relative error in the semilatus rectum is illustrated in Fig. 18. The largest fractional error is  $\sim 50\%$ , this is for  $a \rightarrow 1$  and  $\nu \rightarrow 0$ , and corresponds to small  $p$ , such that the absolute error is still small. Taking the root-mean-square across  $e$  and  $\iota$ , the fractional error for a given  $a_*$  and  $\nu$  never exceeds 9% and is typically less than 4%.

## Appendix B: Asymptotic solution for passage through resonance

The impact of passing through resonance on the evolution can be modelled analytically using asymptotic expansions [56]. Solutions for the motion are constructed far away from resonance and these are matched to a transition region in the vicinity of resonance [33, 57]. By comparing the matched solution, which incorporates the effects of resonance, with the results of an adiabatic evolution, it is possible to estimate the discrepancy in the orbital parameters. This determines the difference in the orbital phase between the two approaches. If this error is sufficiently small, then it is safe to ignore the effects of the resonance; however, only a small difference is needed to impact the subsequent waveform, since the error accumulates over the subsequent observation of  $\sim \mathcal{O}(\eta^{-1})$  cycles [13]. We derive formulae which can be used to calculate the discrepancy in the orbital parameters.

The following derivation is reproduced from Berry [58]. It is based upon the analysis of Kevorkian [40]; small adjustments have been made to adapt to the specific problem of GW inspiral, but the general argument is unchanged.<sup>9</sup> A similar derivation can be found by van de Meent [19].

We model the system using action-angle variables. We are only concerned with the  $r$  and  $\theta$  motions, so we

have a 2-dimensional system. We perform a canonical transformation to isolate the resonant combination  $q = n_r q_r - n_\theta q_\theta$  [19, 33]. This becomes one of the new angle variables, the other variable  $q'$  can be either  $q_r$  or  $q_\theta$  (as, on resonance, varying one necessarily changes the other). We use  $J$  as the conjugate action variable to  $q$  and  $\omega = n_r \omega_r - n_\theta \omega_\theta$  as its frequency. Similarly, we use  $J'$  as the action variable conjugate to  $q'$ . The system evolves through resonance slowly, on an evolution time-scale, so we parameterize it in terms of a slow time parameter

$$\tilde{\lambda} = \eta \lambda. \quad (\text{B1})$$

The orbits of  $q'$  proceed with the fast time  $\lambda$ ; since this is much more rapid than the evolution we are interested in, it is safe to average over it. We are not interested in the fine-grained fast oscillations caused by changes in  $q'$ . For this analysis we consider the reduced problem of evolving  $q$  and  $J$ .

At resonance  $\tilde{\lambda} = \tilde{\lambda}_*$  and  $\omega(\tilde{\lambda}_*) = 0$ . We assume that the frequency has a simple zero and can be expanded as

$$\omega(\tilde{\lambda}) = \varpi_1 (\tilde{\lambda} - \tilde{\lambda}_*) + \varpi_2 (\tilde{\lambda} - \tilde{\lambda}_*)^2 + \dots \quad (\text{B2})$$

The frequency is actually a function of the angle variables, but since these evolve with  $\tilde{\lambda}$  it is safe to write it as a function of the slow time.<sup>10</sup>

Using the slow time, the equations of motion (2) become

$$\frac{dq}{d\tilde{\lambda}} = \frac{\omega(J)}{\eta} + \sum_s g_s^{(1)}(J) \exp(isq) + \mathcal{O}(\eta), \quad (\text{B3a})$$

$$\frac{dJ}{d\tilde{\lambda}} = \sum_s G_s^{(1)}(J) \exp(isq) + \mathcal{O}(\eta), \quad (\text{B3b})$$

where we have rewritten the forcing terms as Fourier series and adapted the forcing functions to those appropriate for  $q$  and  $J$ . We solve these before resonance and then match to solutions in the transition regime about resonance.

### 1. Solution before resonance

To find a solution away from the resonance, we decompose the problem to be a function of two time-scales [57]. We use the slow time  $\tilde{\lambda}$  and, as a proxy for the fast time,

$$\Psi = \int_0^\lambda \omega(\eta\tau) d\tau = \frac{1}{\eta} \int_0^{\tilde{\lambda}} \omega(\tilde{\tau}) d\tilde{\tau}. \quad (\text{B4})$$

From this

$$\omega = \frac{d\Psi}{d\tilde{\lambda}}. \quad (\text{B5})$$

<sup>8</sup> This does not give as good a fit as our function.

<sup>9</sup> The same two time-scale theory underpins the analysis of Hinderer and Flanagan [20], but this explicitly ignores resonances.

<sup>10</sup> In effect we are defining  $\omega(\tilde{\lambda}) \equiv \omega[J(\tilde{\lambda})]$ .

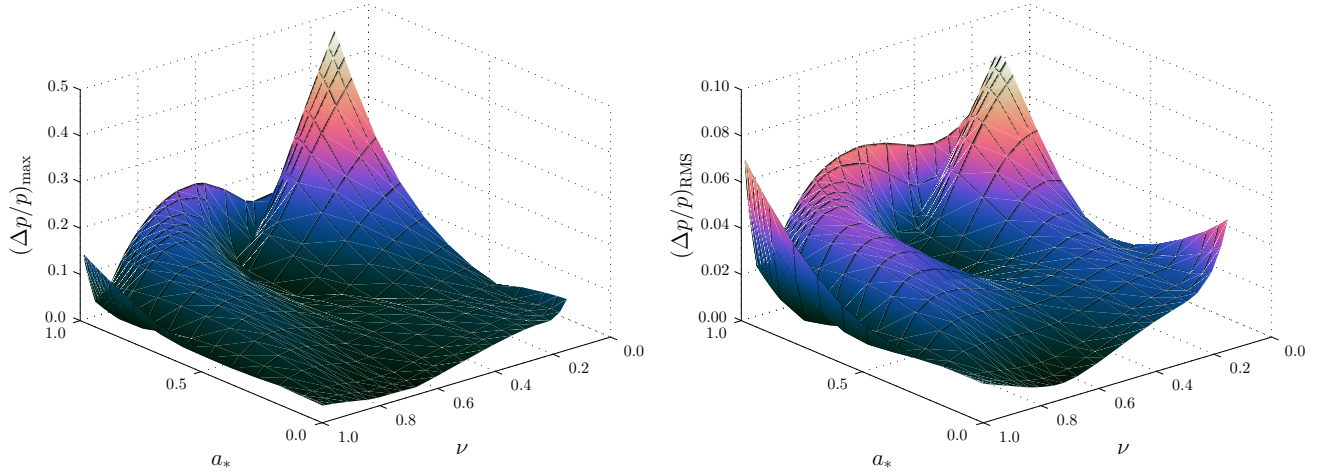


FIG. 18: Relative error in the approximate semilatus rectum compared to the accurate numerical result as a function of BH spin  $a_*$  and resonance ratio  $\nu$ . The left panel shows the maximum relative error and the right shows the root-mean-square error; in both cases we are marginalising over eccentricity and inclination.

In terms of these two variables, we can build ansatz solutions

$$q(\lambda; \eta) = \Psi + q_0(\tilde{\lambda}) + \eta q_1(\Psi, \tilde{\lambda}) + \mathcal{O}(\eta^2), \quad (\text{B6a})$$

$$J(\lambda; \eta) = J_0(\tilde{\lambda}) + \eta J_1(\Psi, \tilde{\lambda}) + \mathcal{O}(\eta^2). \quad (\text{B6b})$$

We can also write a series expansion for the frequency, since it is affected by the self-force too,

$$\omega(\lambda; \eta) = \omega_0(\tilde{\lambda}) + \eta \omega_1(\tilde{\lambda}) + \mathcal{O}(\eta^2). \quad (\text{B7})$$

In the limit of  $\eta \rightarrow 0$  we are left with a constant frequency  $\omega_0(0)$ . The higher-order terms are identified below by

matching terms in the series expansions of the equations of motion. Taking the two time-scales as independent, we may write the time derivative to  $\mathcal{O}(\eta)$  as

$$\frac{d}{d\lambda} = \omega_0 \frac{\partial}{\partial \Psi} + \eta \omega_1 \frac{\partial}{\partial \Psi} + \eta \frac{\partial}{\partial \tilde{\lambda}}. \quad (\text{B8})$$

Using the two time-scale decomposition to replace the time derivatives in the equations of motion, and substituting in the ansatz expansions gives, to first order,

$$\omega_0 + \eta \omega_1 + \eta \frac{\partial q_0}{\partial \tilde{\lambda}} + \eta \omega_0 \frac{\partial q_1}{\partial \Psi} = \omega(J_0) + \eta \frac{d\omega}{dJ} J_1 + \eta \sum_s g_s^{(1)}(J_0) \exp[is(\Psi + q_0)], \quad (\text{B9a})$$

$$\eta \frac{\partial J_0}{\partial \tilde{\lambda}} + \eta \omega_0 \frac{\partial J_1}{\partial \Psi} = \eta \sum_s G_s^{(1)}(J_0) \exp[is(\Psi + q_0)]. \quad (\text{B9b})$$

Averaging (B9b) over  $\Psi$  gives<sup>11</sup>

$$\frac{\partial J_0}{\partial \tilde{\lambda}} = G_0^{(1)}(J_0). \quad (\text{B10})$$

This describes the adiabatic evolution, hence we can identify  $J_0(\tilde{\lambda})$  with (the lowest-order piece of) the adiabatic

solution [20]. If we similarly average (B9a), we find

$$\omega_0 + \eta \omega_1 + \eta \frac{\partial q_0}{\partial \tilde{\lambda}} = \omega(J_0) + \eta \frac{\partial \omega}{\partial J} \langle J_1 \rangle_\Psi + \eta g_0^{(1)}(J_0). \quad (\text{B11})$$

From this we can identify the terms that originate from the frequency and, matching by order in  $\eta$ , obtain

$$\omega_0 = \omega(J_0), \quad (\text{B12a})$$

$$\omega_1 = \frac{\partial \omega}{\partial J} \langle J_1 \rangle_\Psi. \quad (\text{B12b})$$

<sup>11</sup> The ansatz is constructed such that  $J_0 \equiv \langle J_0 \rangle_\Psi$  and  $q_0 \equiv \langle q_0 \rangle_\Psi$ .

This leaves

$$\frac{\partial q_0}{\partial \tilde{\lambda}} = g_0^{(1)}(J_0), \quad (\text{B13})$$

$$q_0 = \kappa_0 + \int_0^{\tilde{\lambda}} g_0^{(1)}[J_0(\tau)] d\tau. \quad (\text{B14})$$

We now have expressions for the lowest-order terms in the expansions.

Subtracting the  $s = 0$  components from (B9b) leaves

$$\omega_0 \frac{\partial J_1}{\partial \Psi} = \sum_{s \neq 0} G_s^{(1)}(J_0) \exp[is(\Psi + q_0)]. \quad (\text{B15})$$

This can be solved to give

$$J_1 = \langle J_1 \rangle_\Psi + \frac{1}{\omega_0} \sum_{s \neq 0} \frac{G_s^{(1)}(J_0) \exp[is(\Psi + q_0)]}{is}. \quad (\text{B16})$$

We can do the same for (B9a) to obtain

$$q_1 = \langle q_1 \rangle_\Psi + \frac{1}{\omega_0} \sum_{s \neq 0} \frac{g_s^{(1)}(J_0) \exp[is(\Psi + q_0)]}{is}. \quad (\text{B17})$$

To find the constants of integration,  $\langle q_1 \rangle_\Psi$  and  $\langle J_1 \rangle_\Psi$ , it is necessary to extend the analysis to second order in  $\eta$ . This shows that  $\langle J_1 \rangle_\Psi$  is the first-order component of the adiabatic solution. We do not need explicit forms for later calculations, so we will not proceed further. We have successfully constructed the pre-resonance solution.

## 2. Solution near resonance

Near to resonance, we consider an interior layer expansion [57]. As explained in Sec. III A, evolution near resonance proceeds on a time-scale intermediate between the slow and fast times. We therefore introduce a rescaled time

$$\hat{\lambda} = \frac{\tilde{\lambda} - \tilde{\lambda}_*}{\eta^{1/2}} = \eta^{1/2}(\lambda - \lambda_*). \quad (\text{B18})$$

As for the before resonance solution, we can create a series expansion; however, now we expand in terms of  $\eta^{1/2}$  [13]

$$q(\hat{\lambda}; \eta) = \hat{q}_0(\hat{\lambda}) + \eta^{1/2} \hat{q}_{1/2}(\hat{\lambda}) + \mathcal{O}(\eta), \quad (\text{B19a})$$

$$J(\hat{\lambda}; \eta) = \hat{J}_0 + \eta^{1/2} \hat{J}_1(\hat{\lambda}) + \mathcal{O}(\eta). \quad (\text{B19b})$$

The series expansion for the frequency, (B2), can be rewritten as

$$\omega(\hat{\lambda}) = \eta^{1/2} \varpi_1 \hat{\lambda} + \eta \varpi_2 \hat{\lambda}^2 + \mathcal{O}(\eta^{3/2}). \quad (\text{B20})$$

Proceeding to write the equations of motion in terms of the rescaled time gives

$$\begin{aligned} \frac{dq}{d\hat{\lambda}} &= \varpi_1 \hat{\lambda} + \eta^{1/2} \varpi_2 \hat{\lambda}^2 \\ &\quad + \eta^{1/2} \sum_s g_s^{(1)}(\hat{J}_0, \tilde{\lambda}_*) \exp(is\hat{q}_0) + \mathcal{O}(\eta), \end{aligned} \quad (\text{B21a})$$

$$\frac{dJ}{d\hat{\lambda}} = \eta^{1/2} \sum_s G_s^{(1)}(\hat{J}_0, \tilde{\lambda}_*) \exp(is\hat{q}_0) + \mathcal{O}(\eta). \quad (\text{B21b})$$

From the equations of motion we can match terms by their order in  $\eta^{1/2}$ . At zeroth order we find

$$\hat{J}_0 = \hat{\varrho}_0 \quad (\text{B22})$$

is constant, and

$$\hat{q}_0 = \hat{\kappa}_0 + \frac{\varpi_1 \hat{\lambda}^2}{2}. \quad (\text{B23})$$

Using these, we can build the next-order terms

$$\begin{aligned} \hat{q}_{1/2} &= \hat{\kappa}_{1/2} + \frac{\varpi_2 \hat{\lambda}^3}{3} + g_0^{(1)}(\hat{\varrho}_0) \hat{\lambda} \\ &\quad + \sum_{s \neq 0} g_s^{(1)}(\hat{\varrho}_0) \exp(is\hat{\kappa}_0) \int_0^{\hat{\lambda}} \exp\left(\frac{is\varpi_1 \tau^2}{2}\right) d\tau, \end{aligned} \quad (\text{B24})$$

$$\begin{aligned} \hat{J}_{1/2} &= \hat{\varrho}_{1/2} + G_0^{(1)}(\hat{\varrho}_0) \hat{\lambda} \\ &\quad + \sum_{s \neq 0} G_s^{(1)}(\hat{\varrho}_0) \exp(is\hat{\kappa}_0) \int_0^{\hat{\lambda}} \exp\left(\frac{is\varpi_1 \tau^2}{2}\right) d\tau. \end{aligned} \quad (\text{B25})$$

Both of these involve the complex Fresnel integral [59], the details of which are given in the following section. We have now constructed the interior solution.

## 3. The complex Fresnel integral

The solution for the motion in the interior region near to resonance involves the integral

$$W(\hat{\lambda}) = \int_0^{\hat{\lambda}} \exp\left(\frac{is\varpi_1 \tau^2}{2}\right) d\tau. \quad (\text{B26})$$

The complex Fresnel integral is

$$\mathcal{Y}(z) = \int_0^z \exp\left(\frac{i\pi x^2}{2}\right) dx = \mathcal{C}(z) + i\mathcal{S}(z), \quad (\text{B27})$$

where  $\mathcal{C}(z)$  and  $\mathcal{S}(z)$  are the cosine and sine Fresnel integrals [59], and hence

$$W(\hat{\lambda}) = \sqrt{\frac{\pi}{s\varpi_1}} \mathcal{Y}\left(\sqrt{\frac{s\varpi_1}{\pi}} \hat{\lambda}\right). \quad (\text{B28})$$

We are interested in the asymptotic behaviour for  $|\hat{\lambda}| \rightarrow \infty$ . The complex Fresnel integral has the limit [59]

$$\lim_{|z| \rightarrow \infty} \mathcal{Y}(z) \sim \frac{\text{sgn } z}{\sqrt{2}} \exp\left(\frac{i\pi}{4}\right) - \frac{i}{\pi z} \exp\left(-\frac{i\pi z^2}{2}\right), \quad (\text{B29})$$

where

$$\text{sgn } z = \begin{cases} 1 & z > 0 \\ -1 & z < 0 \end{cases}. \quad (\text{B30})$$

Hence,

$$\begin{aligned} \lim_{|\hat{\lambda}| \rightarrow \infty} W(\hat{\lambda}) &\sim \frac{\text{sgn } \hat{\lambda}}{\sqrt{2}} \sqrt{\frac{\pi}{|s\varpi_1|}} \exp\left[\text{sgn}(s\varpi_1) \frac{i\pi}{4}\right] \\ &+ \frac{1}{is\varpi_1} \exp\left(\frac{is\varpi_1 \hat{\lambda}^2}{2}\right). \end{aligned} \quad (\text{B31})$$

#### 4. Matching solutions

To complete our solution we must match the pre-resonance solution of Sec. B 1 with the near-resonance solution of Sec. B 2. This is achieved by rewriting the pre-resonance solution in terms of the rescaled time  $\hat{\lambda}$  and comparing this with the near-resonance solution expanded in the limit of  $\hat{\lambda} \rightarrow -\infty$ .

To rewrite the pre-resonance solution, we begin with the fast phase parameter

$$\Psi(\hat{\lambda}) = \frac{\Psi_\star}{\eta} + \frac{\varpi_1 \hat{\lambda}^2}{2} + \eta^{1/2} \frac{\varpi_2 \hat{\lambda}^3}{3} + \mathcal{O}(\eta). \quad (\text{B32})$$

Using this together with equations (B14) and (B17) in (B6a), the angle variable is

$$q(\hat{\lambda}; \eta) = \frac{\Psi_\star}{\eta} + \frac{\varpi_1 \hat{\lambda}^2}{2} + \kappa_\star + \eta^{1/2} \frac{\varpi_2 \hat{\lambda}^3}{3} + \eta^{1/2} g_0^{(1)}(J_\star) \hat{\lambda} + \frac{\eta^{1/2}}{\varpi_1 \hat{\lambda}} \sum_{s \neq 0} \frac{1}{is} g_s^{(1)}(J_\star) \exp\left[is \left(\frac{\Psi_\star}{\eta} + \frac{\varpi_1 \hat{\lambda}^2}{2} + \kappa_\star\right)\right] + \mathcal{O}(\eta), \quad (\text{B33})$$

where we have defined  $J_\star \equiv J_0(\tilde{\lambda}_\star)$  and  $\kappa_\star = \kappa_0 + \int_0^{\tilde{\lambda}_\star} g_0^{(1)}[J_0(\tau)] d\tau$ , and used (B20) to substitute for  $\omega$ . The action variable is similarly determined by using equations (B10) and (B16) with (B6b) to give

$$J(\hat{\lambda}; \eta) = J_\star + \eta^{1/2} G_0^{(1)}(J_\star) \hat{\lambda} + \frac{\eta^{1/2}}{\varpi_1 \hat{\lambda}} \sum_{s \neq 0} \frac{1}{is} G_s^{(1)}(J_\star) \exp\left[is \left(\frac{\Psi_\star}{\eta} + \frac{\varpi_1 \hat{\lambda}^2}{2} + \kappa_\star\right)\right] + \mathcal{O}(\eta). \quad (\text{B34})$$

We can now compare this to the near-resonance expansion with the integral replaced by the limiting form given in (B31).

At zeroth order, we immediately obtain

$$\hat{\kappa}_0 = \frac{\Psi_\star}{\eta} + \kappa_\star, \quad (\text{B35})$$

$$\hat{\varrho}_0 = J_\star. \quad (\text{B36})$$

These fix the integration constants. The more interesting result is now found by comparing the  $\mathcal{O}(\eta^{1/2})$  terms. Equating the angle variable expressions and cancelling terms gives

$$\hat{\kappa}_{1/2} = \sum_{s \neq 0} g_s^{(1)}(\hat{\varrho}_0) \sqrt{\frac{\pi}{2|s\varpi_1|}} \exp\left[i \left(s\hat{\kappa}_0 + \frac{\pi}{4} \text{sgn } s\varpi_1\right)\right]. \quad (\text{B37})$$

Similarly, for the action variables

$$\hat{\varrho}_{1/2} = \sum_{s \neq 0} G_s^{(1)}(\hat{\varrho}_0) \sqrt{\frac{\pi}{2|s\varpi_1|}} \exp\left[i \left(s\hat{\kappa}_0 + \frac{\pi}{4} \text{sgn } s\varpi_1\right)\right]. \quad (\text{B38})$$

We now have a matched solution through resonance.

Having constructed the solution, we see that the lowest-order evolution corresponds to the adiabatic solution; the deviations come in at the following order. When we switch from the pre-resonance solution to the post-resonance solution, there is a change in the sign of  $\hat{\lambda}$ . Therefore, when matching the post-resonance solution  $\hat{\varrho}_{1/2}$  and  $\hat{\kappa}_{1/2}$  also change sign: there is a change of

$$\Delta q = 2\eta^{1/2} \hat{\kappa}_{1/2}, \quad (\text{B39})$$

$$\Delta J = 2\eta^{1/2} \hat{\varrho}_{1/2} \quad (\text{B40})$$

across the resonance [40]. We are not particularly interested in the deviation in  $J$ , of greater concern is the change in the orbital parameters  $\{E, L_z, Q\}$ . Assuming that there is a smooth transformation that maps between  $J$  and these, then, to lowest order, we can calculate the deviation relative to the adiabatic prescription by substituting the forcing functions  $G^{(1)} \rightarrow G_a^{(1)}$ , where  $G_a^{(1)}$  describes the evolution of  $\mathcal{I}_a$  through the effects of the self-force. This result is quoted by Flanagan and Hinderer [13]. The change in the orbital parameters is de-

terminated by the forcing functions, hence it is essential to have an accurate self-force model.

As a final step in understanding our result, we switch from Mino time to coordinate time. An appropriate re-definition of the forcing functions can be done by scaling by  $\Gamma$ , we define

$$F_a^{(1)} = \frac{G_a^{(1)}}{\Gamma}, \quad (\text{B41})$$

such that the equation of motion becomes

$$\left\langle \frac{d\mathcal{I}_a}{dt} \right\rangle_{q'} = \eta \sum_s F_{a,s}^{(1)}(\mathcal{I}) \exp(isq) + \mathcal{O}(\eta^2). \quad (\text{B42})$$

Here we have made the averaging over  $q'$  explicit to show that the equation is only defined as an orbital average: not only does our asymptotic expansion average out oscillations over an orbit in  $q'$ , but in converting from  $\lambda$  to  $t$  we have used  $\Gamma$  which is an orbital average. From (B2), we recognise that

$$\varpi_1 = \frac{\partial \omega}{\partial \tilde{\lambda}} = \frac{\Gamma^2}{\eta} \left\langle \dot{\Omega} \right\rangle_{q'}. \quad (\text{B43})$$

We have used the averaged form of  $\dot{\Omega}(t)$  as this is appropriate. Using these to adapt equations (B38) and (B40), we obtain

$$\begin{aligned} \Delta \mathcal{I}_a &= \eta \sum_{s \neq 0} F_{a,s}^{(1)}(\mathcal{I}_*) \left[ \frac{2\pi}{s \left\langle \dot{\Omega} \right\rangle_{q'}} \right]^{1/2} \\ &\times \exp \left[ i \left( s \hat{\kappa}_0 + \frac{\pi}{4} \text{sgn } s \dot{\Omega} \right) \right] \end{aligned} \quad (\text{B44})$$

$$= \eta \sum_{s \neq 0} F_{a,s}^{(1)}(\mathcal{I}_*) \tau_{\text{res},s} \exp \left[ i \left( s \hat{\kappa}_0 + \frac{\pi}{4} \text{sgn } s \dot{\Omega} \right) \right], \quad (\text{B45})$$

using (28) and representing the values on resonance of  $E$ ,  $L_z$  and  $Q$  with  $\mathcal{I}_*$ .

- 
- [1] S. Chandrasekhar, *The Mathematical Theory of Black Holes*, Oxford Classic Texts in the Physical Sciences (Oxford University Press, Oxford, 1992).
  - [2] F. Pretorius, Physical Review Letters **95**, 121101 (2005), 0507014.
  - [3] M. Campanelli, C. O. Lousto, P. Marronetti, and Y. Zlochower, Physical Review Letters **96**, 111101 (2006), 0511048.
  - [4] J. G. Baker, J. Centrella, D.-I. Choi, M. Koppitz, and J. van Meter, Physical Review Letters **96**, 111102 (2006), 0511103.
  - [5] B. Szilagyi, J. Blackman, A. Buonanno, A. Taracchini, H. P. Pfeiffer, M. A. Scheel, T. Chu, L. E. Kidder, and Y. Pan (2015), 1502.04953.
  - [6] J. Aasi et al., Classical and Quantum Gravity **32**, 074001 (2015), 1411.4547.
  - [7] F. A. et al., Classical and Quantum Gravity **32**, 024001 (2015), 1408.3978.
  - [8] K. Kuroda, Classical and Quantum Gravity **27**, 084004 (2010).
  - [9] P. Amaro-Seoane et al., Classical and Quantum Gravity **29**, 124016 (2012), 1202.0839.
  - [10] P. Amaro-Seoane, J. R. Gair, M. Freitag, M. C. Miller, I. Mandel, C. J. Cutler, and S. Babak, Classical and Quantum Gravity **24**, R113 (2007), 0703495.
  - [11] L. Barack, Classical and Quantum Gravity **26**, 213001 (2009), 0908.1664.
  - [12] E. Poisson, Living Reviews in Relativity **7** (2004), 0306052.
  - [13] É. É. Flanagan and T. Hinderer, Physical Review Letters **109**, 071102 (2012), 1009.4923.
  - [14] H. Goldstein, C. Poole, and J. Safko, *Classical Mechanics* (Pearson Education International, Upper Sadle River, New Jersey, 2002), 3rd ed.
  - [15] A. Pound and E. Poisson, Physical Review D **77**, 044013(18) (2008), 0708.3033.
  - [16] J. R. Gair, É. É. Flanagan, S. Drasco, T. Hinderer, and S. Babak, Physical Review D **83**, 044037 (2011), 1012.5111.
  - [17] E. E. Flanagan, S. A. Hughes, and U. Ruangsri, Physical Review D **89**, 084028 (2014), 1208.3906.
  - [18] C. M. Hirata, Physical Review D **83**, 104024 (2011), 1011.4987.
  - [19] M. van de Meent, Physical Review D **89**, 084033 (2014).
  - [20] T. Hinderer and É. É. Flanagan, Physical Review D **78**, 064028 (2008), 0805.3337.
  - [21] B. Carter, Physical Review **174**, 1559 (1968).
  - [22] Y. Mino, Physical Review D **67**, 084027 (2003), 0302075.
  - [23] S. Drasco, É. É. Flanagan, and S. A. Hughes, Classical and Quantum Gravity **22**, S801 (2005), 0505075.
  - [24] V. I. Arnold, V. Kozlov, and A. I. Neishtadt, in *Dynamical Systems III*, edited by V. I. Arnold (Springer-Verlag, New York, 1988), Encyclopaedia of Mathematical Sciences.
  - [25] R. Grossman, J. Levin, and G. Perez-Giz, Physical Review D **85**, 023012 (2012), 1105.5811.
  - [26] D. Wilkins, Physical Review D **5**, 814 (1972).
  - [27] C. Darwin, Proceedings of the Royal Society A: Mathematical, Physical and Engineering Sciences **263**, 39 (1961).
  - [28] S. Drasco and S. Hughes, Physical Review D **69**, 044015 (2004), 0308479.
  - [29] S. Hughes, Physical Review D **61**, 084004 (2000), 9910091.
  - [30] W. Schmidt, Classical and Quantum Gravity **19**, 2743 (2002), 0202090.
  - [31] F. D. Ryan, Physical Review D **53**, 3064 (1996).
  - [32] K. Glampedakis, S. Hughes, and D. Kennefick, Physical



- Review D **66**, 064005 (2002), 0205033.
- [33] D. L. Bosley and J. Kevorkian, SIAM Journal on Applied Mathematics **52**, 494 (1992).
  - [34] N. Warburton, S. Akcay, L. Barack, J. R. Gair, and N. Sago, Physical Review D **85**, 061501(R) (2012), 1111.6908.
  - [35] V. I. Arnol'd, Russian Mathematical Surveys **18**, 9 (1963).
  - [36] J. Moser, *Stable and Random Motions in Dynamical Systems: With Special Emphasis on Celestial Mechanics*, Annals of mathematical studies (Princeton University Press, Princeton, New Jersey, 1973).
  - [37] É. É. Flanagan and T. Hinderer, Physical Review D **75**, 124007 (2007), 0704.0389.
  - [38] B. R. Iyer and C. M. Will, Physical Review Letters **70**, 113 (1993).
  - [39] L. E. Kidder, Physical Review D **52**, 821 (1995), 9506022.
  - [40] J. Kevorkian, SIAM Review **29**, 391 (1987).
  - [41] S. Babak, H. Fang, J. R. Gair, K. Glampedakis, and S. A. Hughes, Physical Review D **75**, 024005 (2007), 0607007.
  - [42] C. P. L. Berry and J. R. Gair, Monthly Notices of the Royal Astronomical Society **429**, 589 (2013), 1210.2778.
  - [43] C. W. Misner, K. S. Thorne, and J. A. Wheeler, *Gravitation* (W. H. Freeman, 1973).
  - [44] C. J. Moore, R. H. Cole, and C. P. L. Berry, Classical and Quantum Gravity **32**, 015014(25) (2015), 1408.0740.
  - [45] D. J. A. McKechnan, C. Robinson, and B. S. Sathyaprakash, Classical and Quantum Gravity **27**, 084020 (2010).
  - [46] C. Cutler and M. Vallisneri, Physical Review D **76**, 104018 (2007).
  - [47] L. Barack and C. Cutler, Physical Review D **69**, 082005 (2004).
  - [48] J. R. Gair, L. Barack, T. Creighton, C. Cutler, S. L. Larson, E. S. Phinney, and M. Vallisneri, Classical and Quantum Gravity **21**, S1595 (2004), 0405137.
  - [49] C. Hopman, Classical and Quantum Gravity **26**, 094028 (2009), 0901.1667.
  - [50] P. Amaro-Seoane and M. Preto, Classical and Quantum Gravity **28**, 094017 (2010), 1010.5781.
  - [51] J. E. Greene and L. C. Ho, The Astrophysical Journal **667**, 131 (2007), 0705.0020.
  - [52] J. R. Gair, C. Tang, and M. Volonteri, Physical Review D **81**, 104014 (2010), ISSN 15507998, 1004.1921.
  - [53] C. Hopman and T. Alexander, The Astrophysical Journal **629**, 362 (2005).
  - [54] J. R. Gair, Classical and Quantum Gravity **26**, 094034 (2009), 0811.0188.
  - [55] J. Brink, M. Geyer, and T. Hinderer, Physical Review Letters **114**, 081102 (2015), 1304.0330.
  - [56] J. Gair, N. Yunes, and C. M. Bender, Journal of Mathematical Physics **53**, 032503 (2012), 1111.3605.
  - [57] J. Kevorkian, SIAM Journal on Applied Mathematics **20**, 364 (1971).
  - [58] C. P. L. Berry, Ph.D. dissertation, University of Cambridge (2013), URL <http://www.repository.cam.ac.uk/handle/1810/245139>.
  - [59] F. W. J. Olver, W. Lozier, Daniel, R. F. Boisvert, and C. W. Clark, eds., *NIST Handbook of Mathematical Functions* (Cambridge University Press, Cambridge, 2010).